

Rochester Institute of Technology

## RIT Digital Institutional Repository

---

Theses

---

9-30-1991

### Determination of impeller pumping capacity from laser doppler anemometer (LDA) measurements in an agitated vessel

Mark Iamonaco

Follow this and additional works at: <https://repository.rit.edu/theses>

---

#### Recommended Citation

Iamonaco, Mark, "Determination of impeller pumping capacity from laser doppler anemometer (LDA) measurements in an agitated vessel" (1991). Thesis. Rochester Institute of Technology. Accessed from

This Thesis is brought to you for free and open access by the RIT Libraries. For more information, please contact [repository@rit.edu](mailto:repository@rit.edu).

**DETERMINATION OF IMPELLER PUMPING  
CAPACITY FROM  
LASER DOPPLER ANEMOMETER (LDA)  
MEASUREMENTS IN AN AGITATED VESSEL**

**by  
Mark A. Iamonaco**

**A Thesis Submitted  
in  
Partial Fulfillment  
of the  
Requirements for the Degree of**

**MASTER OF SCIENCE  
in  
Mechanical Engineering**

Approved by:

Prof. Ali Ogut

(Thesis Advisor)

Prof. Alan H. Nye

Prof. R. J. Hefner

Prof. C. Harris

(Department Head)

**DEPARTMENT OF MECHANICAL ENGINEERING  
COLLEGE OF ENGINEERING  
ROCHESTER INSTITUTE OF TECHNOLOGY  
ROCHESTER, NEW YORK**

1. Title of thesis Determination of Impeller Pumping Capacity from Laser Doppler Anemometer (LDA) Measurements in an Agitated Vessel  
I \_\_\_\_\_ hereby **grant permission** to the

Wallace Memorial Library of RIT to reproduce my thesis in whole or in part. Any reproduction will not be for commercial use or profit.

Date 9/30/1991

2. Title of thesis \_\_\_\_\_  
\_\_\_\_\_

I \_\_\_\_\_ **prefer to be contacted** each time a request for reproduction is made. I can be reached at the following address.

\_\_\_\_\_  
\_\_\_\_\_

Date \_\_\_\_\_

3. Title of Thesis \_\_\_\_\_  
\_\_\_\_\_

I \_\_\_\_\_ hereby **deny** permission to the

Wallace Memorial Library of RIT to reproduce my thesis in whole or in part.

Date \_\_\_\_\_

## **ACKNOWLEDGMENT**

The author wishes to thank Dr. Ali Ogut & David Hathaway for their guidance and assistance throughout this project.

The author also wishes to thank his family and friends for their hope and financial support.

## 1.0 ABSTRACT

The purpose of this thesis was to study fluid mixing by determining impeller pumping capacities from measured velocities in a mixing tank. Mean velocity measurements were made with the use of a Laser Doppler Anemometer (LDA). The LDA was operated in the dual beam mode, with polystyrene spheres as seeding material. Studies were conducted with a 6 blade radial impeller and a 3 blade axial impeller.

From velocity measurements, impeller pumping capacities were calculated for the above impellers. Impeller pumping capacities are correlated for varying impeller speeds at various measurement positions. The obtained results have been compared to published results under similar conditions.

## TABLE OF CONTENTS

	<u>PAGE</u>
LIST OF TABLES	5
LIST OF FIGURES	6
LIST OF SYMBOLS	8
1.0 INTRODUCTION	10
2.0 THEORY AND LITERATURE SEARCH	12
3.0 MATERIALS AND METHODS	26
4.0 RESULTS AND DISCUSSION	41
5.0 CONCLUSIONS	74
6.0 APPENDIX	75
7.0 BIBLIOGRAPHY	88

## LIST OF TABLES

<b>Table</b>	<b>Title</b>	<b>Page</b>
I.	Methods of Seeding	36
II.	Impeller Tip Speed Comparison to Maximum Fluid Velocity	61

## LIST OF FIGURES

Figure	Title	Page
1.	Flow Pattern Induced by a Radial Impeller	12
2.	Flow Pattern Induced by an Axial Impeller	13
3.	Control Surface for Calculating the Pumping Capacity	14
4.	Turbine Design Affects on Power Requirements for Agitated Systems	23
5.	Variation of Drag Coefficient with Aspect Ratio	24
6.	Impeller Streamline Flow Pattern	25
7.	Torquemeter Calibration Curve	29
8.	LDA Velocity Vectors	32
9.	Dual Beam Mode	33
10.	Fringe Model	34
11.	Axial Velocity Profiles (Runs for Jun5 at Q)	42
12.	Axial Velocity Profiles (Runs for Jun5 at H)	43
13.	Axial Velocity Profiles (Runs for Jun5 at O)	44
14.	Axial Velocity Profiles (Weetman and Oldshue)	45
15.	Axial Velocity Profiles (Weetman and Salzman)	45
16.	Velocity Vectors in the $R_z$ Plane (Oldshue)	46
17.	Axial Velocity Profiles (Jun52ax runs)	47
18.	Axial Velocity Profiles (Jun53ax runs)	48
19.	Axial Velocity Profiles (Jun55ax runs)	49
20.	Axial Velocity Profiles (Jun57ax runs)	50
21.	Radial Velocity Profiles (Runs for Jun7 at Q)	52
22.	Radial Velocity Profiles (Runs for Jun7 at H)	53
23.	Radial Velocity Profiles (Runs for Jun7 at O)	54
24.	Radial Velocity Profiles (Oldshue)	55
25.	Radial Velocity Profiles (Jun 72 runs)	56
26.	Radial Velocity Profiles (Jun 73 runs)	57
27.	Radial Velocity Profiles (Jun 75 runs)	58
28.	Radial Velocity Profiles (Jun 77 runs)	59
29.	Radial Profile Deterioration as a Function of $R_s$	60
30.	Radial Velocity Profiles Generated by a Rushton Turbine	60
31.	Axial Pumping Capacity Area's of Study	62

32.	Axial Pumping Capacity vs. N (Range = Impeller Blade Length)	63
33.	Axial Pumping Capacity vs. N (Extended Range)	64
34.	Radial Pumping Capacity Area's of Study	67
35.	Radial Pumping Capacity vs. N (Range = Impeller Blade Height)	68
36.	Radial Pumping Capacity vs. N (Extended Range)	69
37.	Power vs. Impeller Speed (Experimental)	71
38.	Power vs. Impeller Speed (Historical)	72
39.	$N_P$ vs $N_{Re}$ for Open Impellers	72
40.	$N_P$ vs. $N_{Re}$ for Various Impeller Diameters	73

## LIST OF SYMBOLS

<b>Symbol</b>	<b>Description</b>
A	Area, m <sup>2</sup>
D	Impeller Diameter, m
D/Dt	Substantial Time Derivative
e <sub>i</sub>	Incident Light Unity Vector
e <sub>s</sub>	Scattered Light Unity Vector
F	Force, N
f <sub>d</sub>	Doppler Shift Frequency, Hz
f <sub>i</sub>	Frequency of Incident Light, Hz
f <sub>s</sub>	Frequency of Scattered Light, Hz
g	Acceleration of Gravity, m/s <sup>2</sup>
g <sub>c</sub>	Gravitation Conversion Constant, m/s <sup>2</sup>
K	Constant
K <sub>L</sub>	Constant
K <sub>T</sub>	Turbine Discharge Coefficient
n	Exponent
N	Impeller speed, rps
N <sub>FR</sub>	Froude Number
N <sub>P</sub>	Power Number
N <sub>PR</sub>	Prandtl Number
N <sub>Pviscous</sub>	Viscous Power Number
N <sub>Q</sub>	Flow Number
N <sub>Re</sub>	Reynolds Number
p	Pressure, Pa
p <sub>o</sub>	Reference Pressure, Pa
p*	Dimensionless Pressure
p**	Dimensionless Pressure
P	Power, W
Q	Pumping Capacity, m <sup>3</sup> /s
Q <sub>ax</sub>	Axial Pumping Capacity, m <sup>3</sup> /s
Q <sub>rad</sub>	Radial Pumping Capacity, m <sup>3</sup> /s
R <sub>s</sub>	Impeller Radius, m
t	Time, sec.

$T$	Tank Diameter, m
$t^*$	Dimensionless Time Component
$TT$	Torque, Nm
$u$	Velocity Along the x Axis, m/s
$v$	Velocity Along the y Axis, m/s
$V$	Velocity (u,v,w), m/s
$V_{Max}$	Maximum Velocity, m/s
$V_R$	Radial Mean Velocity, m/s
$V_Z$	Axial Mean Velocity, m/s
$v^*$	Dimensionless Velocity
$W$	Impeller Blade Width, m
$w$	Velocity Along the z Axis, m/s
$x$	X Position Component, m
$x^*$	Dimensionless X Position Component
$y$	Y Position Component, m
$y^*$	Dimensionless Y Position Component
$z$	Z Position Component, m
$z^*$	Dimensionless Z Position Component
$\mu$	Viscosity, m <sup>2</sup> /s
$\rho$	Density, kg/m <sup>3</sup>
$\delta f$	Fringe Spacing, nm
$\lambda$	Incident Light Wavelength, nm
$\phi$	Angle Between the Incident and Scattered Laser Beams
$\nabla$	Vector Differential Operator
$\nabla^*$	Dimensionless Differential Operator
$\nabla^2$	Laplacian Operator
$\nabla^{*2}$	Dimensionless Laplacian Operator

## 1.0 INTRODUCTION

Fluid mixing is an integral part of many industrial processes. It is important to the chemical, food, mining, paper, pharmaceutical, and petroleum industries. Despite the great number of industries dependent upon mixing, the theoretical base is still rather underdeveloped. This is primarily due to the fact that the flow is complex, and the mixing processes are not well understood.

The term mixing is applied to any process which tends to reduce the degree of non-homogeneity in composition, property, or temperature of a bulk mass. The mixing process is accomplished through a combination of bulk flow in both the laminar and turbulent regimes and also through eddy and molecular diffusion. Therefore, two principle actions of fluid motion occur in the mixing process. The first being bulk or macroscopic motion, the second being microscopic motion associated with turbulence.

The most straightforward approach to the study of fluid mixing is through the principles of fluid mechanics. The mixing process occurs through mass diffusion and fluid motion. Convection currents between the various molecular constituents of the fluid are set in motion by natural diffusion. Forced convection may be set in place through the application of mechanical energy. Mechanical energy can be applied through the use of a mixer.

A fluid mixer is a device which consists of a drive system with a shaft, and one or more impellers attached to the shaft. The rotation of the impellers promotes the macroscopic and microscopic fluid motion which satisfies the process requirements.

Applications of the mixing process vary and include, the blending of low and high viscosity fluids, the suspension of solids in liquids, the dispersion of solids or gases in liquids, and the process of heat transfer.

The motivation behind this work was the desire to study impeller generated flow patterns using an LDA, and to compare axial and radial impeller performances through the impeller pumping capacities.

## 2.0 THEORY & LITERATURE SEARCH

Fluid mixing is one of the unit operations in the chemical industry. The primary objective is the desire to generate motion to add homogeneity to liquid-liquid, liquid-solid, liquid-gas, or gas-liquid-solid systems. This motion is generated through the use of impellers which are characterized by the type of flow pattern they generate, the amount of flow they pump and the amount of power they draw.

### 2.1 IMPELLER TYPES

Two types of impellers are used for the majority of all mixing applications. They are classified as radial and axial. Each impeller is characterized by the type of fluid flow it generates. An axial impeller generates axial flow while a radial impeller generates radial flow.

Impeller types most often used in fluid mixing processes are shown in Appendix A.

#### 2.1.1 Radial Flow Impellers

A radial flow impeller generates fluid flow in a radial direction from the impeller tip towards the wall of the mixing tank. Top to bottom flow is also generated if the mixing tank is equipped with baffles. Figure 1 illustrates the typical flow generated by a radial impeller.

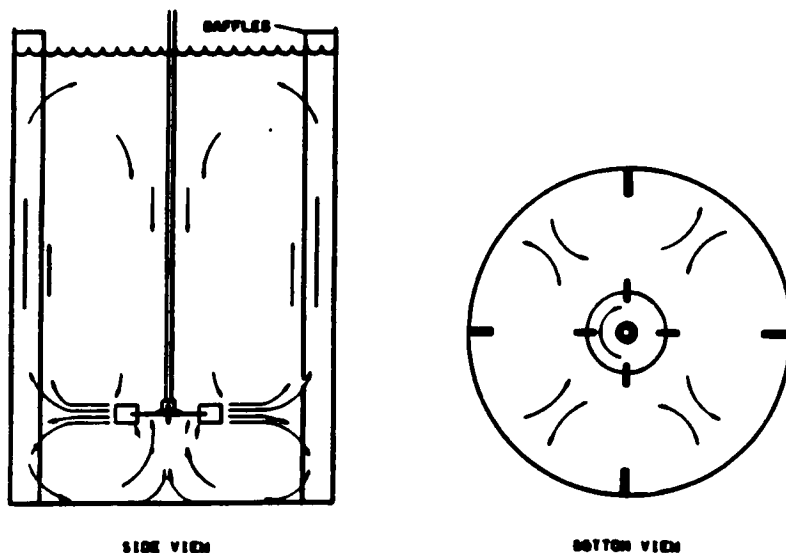
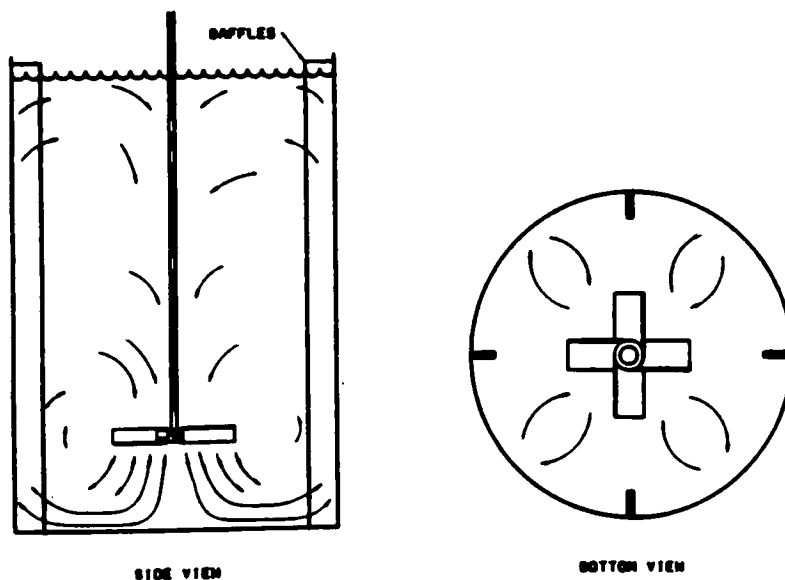


Figure 1: Flow Pattern Induced by a Radial Impeller

In separate studies Cooper and Wolf (3), Weetman and Oldshue (21), Weetman and Salzman (20), and Oldshue (12) have shown that velocity profiles generated by a radial impeller take the form as described in Figure 1. Furthermore, Cooper and Wolf (3) and Sachs and Rushton(18) have shown that radial velocity profiles become flatter in nature as the radial distance from the impeller tip is increased; while Weetman and Salzman (20) and Oldshue (13) have shown that the maximum value of a radial velocity profile increases as the impeller speed is increased.

### 2.1.2 Axial Flow Impellers

An axial flow impeller predominantly generates flow in a direction parallel to the axis of impeller rotation. The flow generated by an axial impeller can circulate in a top to bottom or bottom to top cycle depending upon the orientation of the blades. Figure 2 reveals top to bottom fluid motion as generated by a top to bottom configured axial flow impeller.



**Figure 2: Flow Pattern Induced by an Axial Impeller**

Weetman and Oldshue (21), Weetman and Salzman (20), and Oldshue (13) have also shown that axial velocity profiles take the form as shown in Figure 2. Furthermore, these investiga-

tions revealed that the majority of the flow generated by the impeller occurs in the area closest to the impeller blades, the so called "impeller zone".

## 2.2 PUMPING CAPACITY

As an impeller rotates it acts like a pump and generates fluid motion throughout the tank. This pumping action propagates throughout the tank by momentum transfer.

Pumping Capacity,  $Q$ , is defined as the volumetric flow rate leaving the impeller blades. This volumetric flowrate can be found by calculating the area under an impeller's velocity profile.

Consider the control volume shown in Figure 3:

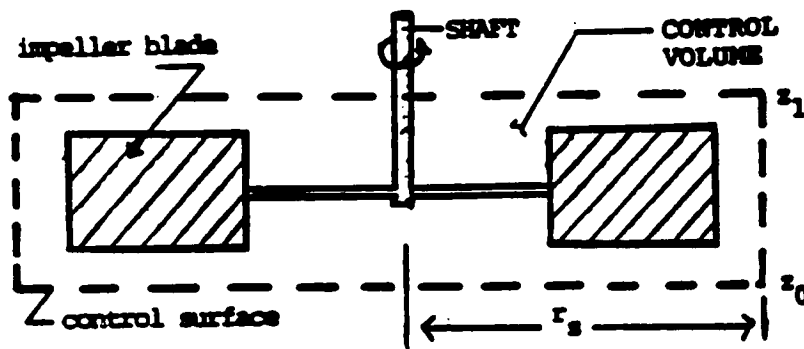


Figure 3: Control Surface For Calculating the Impeller Pumping Capacity

By integrating the mean velocities with respect to the radial direction, the axial pumping capacity can be found to be:

$$Q_{ax} = 4\pi \int_0^{r_s} r \bar{V}_z dr \quad (1)$$

By integrating the mean velocities with respect to the axial direction, the radial pumping capacity can be found to be:

$$Q_r = 2\pi r_S \int_{z_0}^{z_1} \vec{V}_r dz \quad (2)$$

In the late 1940's Rushton, Mack, and Everett (17) studied pumping capacities with the use of a 2 tank set-up which utilized a propeller driven pumping force. These authors described the axial pumping rate as:

$$Q_{ax} = KND^2 \quad (3)$$

where:

K = Constant

N = Impeller speed

D = Impeller diameter

In 1953, Rushton and Oldshue (16) reported the axial pumping rate to be dependent upon the cube of the impeller diameter with a K value of 0.4 for water at 70<sup>0</sup> F.

$$Q_{ax} = .4ND^3 \quad (4)$$

In 1963 Marr and Johnson (10) conducted a pumping capacity experiment with the use of a "flow follower". The flow follower was a rubber plug which travelled about the mixing tank within the impeller stream. By analyzing the time it took the flow follower to travel a specified distance about the tank, the velocity and eventually the pumping rate was obtained. They determined Q to be represented by:

$$Q_{ax} = 0.7ND^3 \quad (5)$$

Subsequent work by Marr and Johnson(10) found Q to take the form of:

$$Q_{ax} = .61ND^3 \quad (6)$$

In 1966 Cooper (3) derived an expression to approximate the radial pumping rate. He found this expression to be:

$$Q_{\text{rad}} = K_t N D^3 \quad (7)$$

Where the value of  $K_t$  varied between .95 and 1.17 depending on turbine diameter and mixing fluid.

Gray (6) has also shown that  $Q_{\text{rad}}$  takes the form as described in Equation 7; with the exception that  $K_t$  was found to vary between 0.5 and 2.9 depending turbine diameter and fluid mixing system.

These findings, however, do not take into effect how much power a radial impeller draws versus an axial impeller. To accurately compare the two impellers, the power consumption of each must be determined.

### 2.3 POWER CONSUMPTION

Power consumption is an important characteristic of an impeller. The expression for the power consumption can be obtained from the Navier–Stokes equation. For a Newtonian fluid with constant density, the Navier–Stokes equation takes the following form:

$$\rho \frac{D\vec{v}}{Dt} = -\nabla p + \mu \nabla^2 \vec{v} + \rho \vec{g} \quad (8)$$

The first, second, third, and fourth terms in the Naviers Stokes equation represent inertial, pressure, viscous, and gravitational forces respectively. By combining the variables in Equation (8) into dimensionless groups, the number of independent quantities describing the equation can be reduced. This simplification is carried out by substituting dimensionless variables, which are the ratios of the actual variables to characteristic variables, into the Equation 8.

The principle dimensions of length, time, and mass are selected to represent the characteristic variables. The impeller diameter,  $D$ , is chosen as the characteristic length quantity. The reciprocal of the impeller speed,  $1/N$ , is the characteristic time dimension, while the

product of the fluid density,  $\rho$ , and the cube of the impeller diameter,  $D^3$ , is the characteristic mass quantity.

Dimensionless variables are described as any variable raised to the starred (\*) power. For example, dimensionless lengths and times are defined as:

$$\begin{aligned}x^* &= x/D \\y^* &= y/D \\z^* &= z/D \\t^* &= tN\end{aligned}\tag{9}$$

While dimensionless velocity and dimensionless pressures are:

$$\begin{aligned}\vec{v}^* &= \frac{\vec{v}}{ND} \\p^* &= p/(\rho N^2 D^2)\end{aligned}\tag{10}$$

Recalling that the Del operator,  $\nabla$ , represents:

$$\nabla = \frac{\delta}{\delta x_i} + \frac{\delta}{\delta x_j} + \frac{\delta}{\delta x_k}\tag{11}$$

and utilizing (9) from above:

$$\begin{aligned}x^* &= x/D, \quad x = x^*D \\y^* &= y/D, \quad y = y^*D \\z^* &= z/D, \quad z = z^*D\end{aligned}\tag{12}$$

Del becomes:

$$\nabla = \frac{\delta}{\delta x^* D} + \frac{\delta}{\delta y^* D} + \frac{\delta}{\delta z^* D} \quad (13)$$

$$\nabla = \frac{1}{D} \left( \frac{\delta}{\delta x^*} + \frac{\delta}{\delta y^*} + \frac{\delta}{\delta z^*} \right) \quad (14)$$

or synonymously:

$$\nabla = \frac{1}{D} (\nabla^*) \quad (15)$$

Along the same lines  $\nabla^2$  can be shown to be:

$$\nabla^2 = \frac{1}{D^2} (\nabla^{*2}) \quad (16)$$

Using Equation (8) with Equations (9), (10), and (11) we see that:

$$\rho \frac{D\vec{v}}{Dt} = - \nabla p + \mu \nabla^2 \vec{v} + \rho \vec{g} \quad (8)$$

is equal to:

$$\rho \frac{DN^2 D\vec{v}^*}{Dt^*} = - \nabla ( \rho N^2 D^2 p^* ) + \mu \nabla^2 N D\vec{v}^* + \rho \vec{g} \quad (17)$$

Equation 18 is further simplified by removing all constant values from differential operations:

$$\rho N^2 D \left( \frac{D\vec{v}^*}{Dt^*} \right) = - \nabla p^* ( \rho N^2 D^2 ) + \mu N D \nabla^2 \vec{v}^* + \rho \vec{g} \quad (18)$$

By employing Equations (15) and (16) in the above equation, we see:

$$\rho N^2 D \left( \frac{D\vec{v}^*}{Dt^*} \right) = -\nabla^* p^* (\rho N^2 D) + \frac{\mu N \nabla^{*2} \vec{v}^*}{D} + \rho \vec{g} \quad (19)$$

By dividing both sides of Equation (19) by  $\rho N^2 D$ , it reduces to the following differential form:

$$\frac{D\vec{v}^*}{Dt^*} = -\nabla^* p^* + \frac{\mu}{ND^2 \rho} \nabla^{*2} \vec{v}^* + \frac{\vec{g}}{N^2 D} \quad (20)$$

In Equation (20) two dimensionless groups appear as parameters. The reciprocal of the Reynolds Number for agitation,  $N_{Re} = D^2 N \rho / \mu$ , and the reciprocal of the Froude Number for agitation,  $N_{Fr} = N^2 D / g$ . The Reynolds Number represents the ratio of inertial to viscous terms, while the Froude Number represents the ratio of inertial to gravitational forces.

Thus Equation (20) takes a final form of:

$$\frac{D\vec{v}^*}{Dt^*} = -\nabla^* p^* + \frac{1}{N_{Re}} \nabla^{*2} \vec{v}^* + \frac{1}{N_{Fr}} \quad (21)$$

Analysis of Equation (21) reveals the basic relationship for velocity and pressure. For a given set of initial and boundary conditions, velocity and pressure distributions from the solution of Equation (21) can be described as functions of the Reynold's and Froude numbers.

$$\vec{v}^*(x^*, y^*, z^*, t^*) = f(N_{Re}, N_{Fr}) \quad (22)$$

$$p^*(x^*, y^*, z^*, t^*) = f(N_{Re}, N_{Fr}) \quad (23)$$

When the liquid surface is essentially flat, such as in fully baffled tanks, the gravitational effects can be eliminated. This implies that the Froude number,  $N_{Fr}$ , will have a negligible effect on the velocity or pressure distributions. Therefore, the velocity and pressure distributions can be determined solely by the magnitude of the Reynolds number.

### 2.3.1 Agitator Power

The pressure distribution acting along the face of an impeller blade can be related to the power requirements of the impeller. Recalling that power is the product of rotational speed and applied torque,  $P = TN$ ; while torque is the product of the applied force and the distance to the axis of rotation,  $T = FR_s$  we can write:

$$F = pA \quad A = \text{Blade Surface Area} \quad (24)$$

Then:

$$T = pAR_s \quad R_s = \text{Distance to the impeller axis of rotation} \quad (25)$$

While power becomes:

$$\text{Power} = pAR_sN \quad (26)$$

Since ( $A \propto D^2$ , and  $R_s \propto D$ ), then  $p$  can be described as:

$$p = \text{Power}/(D^3N) \quad (27)$$

Using Equation (10) together with Equation (27),  $p^*$  becomes:

$$p^* = P/(D^5N^3\rho) \quad P = \text{Power} \quad (28)$$

Equation (28) describes dimensionless pressure in terms of power and is referred to as the power number,  $N_p$ .

$$N_p = P/(D^5N^3\rho) \quad (29)$$

## 2.3.2 Limiting Cases

### 2.3.2.1 Large Reynolds Numbers

Using Equation (21) and the fact that gravitational effects can be eliminated, the limiting cases for agitator power requirements can be studied. Large values of the Reynolds Number indicate turbulent agitation where viscous forces are found to be negligible when compared to inertial forces.

Utilizing this fact the Navier Stokes equation becomes an equivalence between inertial and pressure forces:

$$\frac{D\vec{v}^*}{Dt^*} = -\nabla^* p^* \quad (30)$$

Since the Reynolds number is no longer a variable, the pressure and velocity distributions are fixed for this case. A fixed pressure distribution along the impeller blade means that, at high Reynolds Numbers the Power Number becomes constant.

$$P/(\rho N^3 D^5) = \text{Constant} \quad (31)$$

$$N_P = P / \rho N^3 D^5 \quad (32)$$

(Equation (32) is referred as the inertial power number)

### 2.3.2.2 Small Reynolds Numbers

The second limiting case refers to instances where the Reynolds Number is very small, therefore, inertial and gravitational forces become negligible and viscous forces dominate. As a result, the Navier Stokes equation becomes an equivalence between pressure and viscous forces:

$$\nabla^* p^* = \frac{\mu}{ND^2 \rho} \nabla^{*2} \vec{v}^* \quad (33)$$

Analysis of Equation (33) is done with a new form of dimensionless pressure. The characteristic pressure is related to viscous force per unit area, since momentum has been neglected such that:

$$p^{**} = p/(\mu N) \quad (34)$$

Using Equation (34), Equation (33) can be written as:

$$\frac{\nabla^* p}{\rho N^2 D^2} = \frac{\mu \nabla^{*2} \vec{v}^*}{ND^2 \rho} \quad (35)$$

$$\nabla^* p^{**} = \nabla^{*2} \vec{v}^* \quad (36)$$

As shown in Equation (36) the Reynolds number has again been eliminated as a parameter, and the velocity and pressure distributions are again constant.

Substituting Equation (27) into Equation (36) will further reveal that  $p^{**}$  can be described as:

$$p^{**} = (P/D^3 N)/\mu N \quad (37)$$

$$p^{**} = \frac{P}{\mu D^3 N^2} \quad (38)$$

Equation (38) is referred to as the viscous power number, since it is constant in the viscous range.

$$N_{P_{\text{viscous}}} = P/(\mu N^2 D^3) \quad (39)$$

Rearranging Equation (39) shows that power can be represented by the form:

$$\text{Power} = \mu N^2 D^3 \quad (40)$$

The relationship between Power Number and Reynolds Number for four impeller configurations is shown in Figure 4. In this figure the laminar, the transition, and the turbulent liquid ranges are shown. The laminar range occurs below Reynolds Numbers of about

20 where the power number is a function of one over the Reynolds Number, while the turbulent range occurs at Reynolds Numbers above approximately 10,000 where the power number is relatively constant. The range between 20 and 10,000 is the transition region.

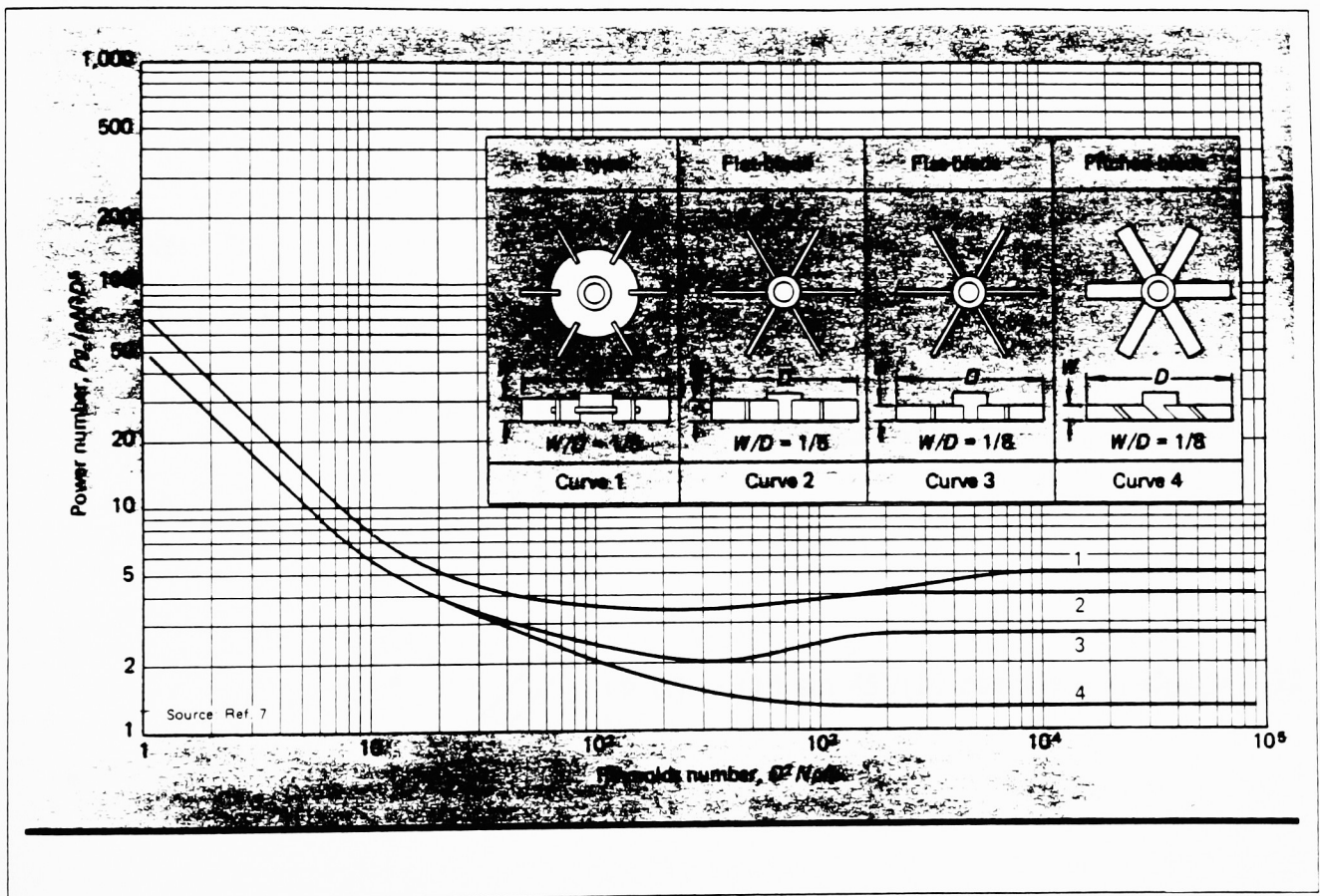


Figure 4: Turbine Design Affects on Power Requirements for Agitated Systems

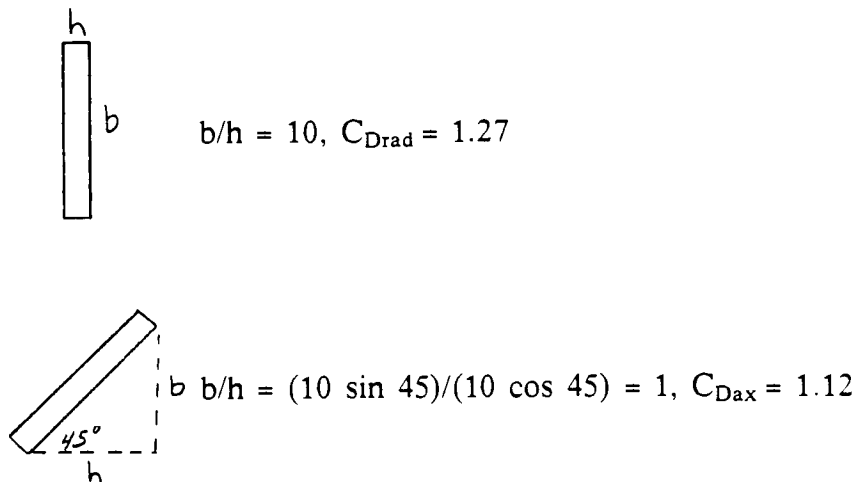
## 2.4 DRAG FORCE COMPARISONS

The power which an impeller draws is due to the pressure drag exerted on the impeller blades by the fluid medium. The radial impeller encounters a higher pressure drag force than the axial impeller due to the fact that more of its blade surface area is normal to the fluid flow.

The variation of drag coefficient with aspect ratio ( $b/h$ ) for each impeller type is shown in Figure 5. In this case the radial impeller drag coefficient is shown to be 8% greater than the axial impeller drag coefficient value.

Example:

$$b = 10, h = 1$$

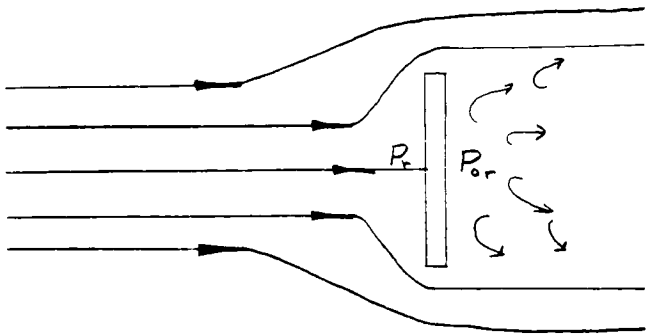


$$C_{D_{rad}} / C_{D_{ax}} = 1.13$$

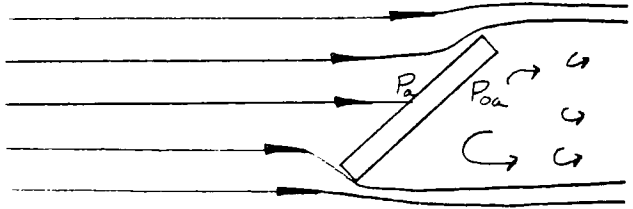
**Figure 5: Variation of Drag Coefficient with Aspect Ratio**

(Drag coefficient vs aspect ratio courtesy of Hoerner, Fluid Dynamic Drag, 2nd Edition, 1965)

The streamline flow pattern over each type of impeller blade is shown in Figure 6. The radial impeller having a larger wake and a subsequently larger pressure value, is shown to generate a larger drag force than the axial impeller.



$$\text{Drag} = P_r - P_{or}$$



$$\text{Drag} = P_a - P_{oa}$$

$$(P_r - P_{or}) > (P_a - P_{oa})$$

Radial Impeller Drag > Axial Impeller Drag

**Figure 6: Impeller Streamline Flow Pattern**

Based upon the data shown in the previous two figures, a radial impeller with similar aspect ratio characteristics to an axial impeller would require more power to operate under identical conditions, since it operates under a larger drag force than does the axial impeller. It should be noted, however, that in some types of mixing applications the cost of added input power is outweighed by the benefits of pumping rate, and fluid flow pattern generation.

## 3.0 MATERIALS AND METHODS

### 3.1 FLUID MIXING SYSTEM

The mixing station used in this study consisted of two tanks filled with water, one being tubular, and the other being rectangular and enclosing the tubular tank. The actual mixing process takes place in the tubular tank, while the rectangular tank is used to decrease the effects of laser light defraction.

The height of the tank system is 3.0 times the tubular tank diameter. The tubular tank is fitted with 4 baffles which are placed at 90<sup>0</sup> increments to one another. The baffles are principally used to enhance turbulence within the tubular tank.

A baffled tank is characterized by: 1) Top to bottom turnover with complete mixing throughout the tank, 2) the absence of vorticity which draws air into the impeller stream, and 3) the absence of a swirling pattern caused by the vortex.

In most cases a baffled pattern is desirable. Unbaffled patterns cause severe fluid forces which act against the impeller and impeller shaft. In some applications, however, partially baffled or unbaffled systems are employed. These cases occur when it is desirable to utilize the vortex action to draw liquids or fluids from the surface into the impeller stream.

The two tank set-up was supported by a metal pedestal. The pedestal added stability and ease of access to the mixing tanks.

The tubular tank was filled with fluid to a height equal to the tank diameter. Mixing of this fluid was carried out with the use of an impeller, with a diameter equal to 30 to 70 percent of the tubular tank diameter. The impeller was fitted to the end of a shaft which ran through a torquemeter, to a variable speed motor. A schematic diagram of the system is shown in Appendix C, under the heading "Detailed Mixing Station Design Drawings".

### **3.1.1 Tank**

A complete drawing showing all pertinent dimensions for tank and system components is given in Appendix C.

The tubular tank diameter had an outside diameter (O.D.) of 8 inches and a height of 24 inches; while the dimensions of the rectangular tank were 12.75 inches X 12.75 inches X 26 inches.

### **3.1.2 Tank Pedestal**

The tank pedestal was designed to support the mixing tank and to allow for ease of access to the drain valves installed in the base of each tank. Four steel legs were welded below the base so that the pedestal could be secured to a table top.

### **3.1.3 Wall Cantilever**

This structure was built to rigidly support the d.c. motor and torquemeter. The wall cantilever bearing was attached to the cantilever support in order to support and position the impeller shaft. The wall cantilever was designed so that the vertical position of the D.C. motor and torquemeter could be adjusted.

### **3.1.4 Cantilever Bearing**

Two bearing arrangements were designed to dampen vibrations in the impeller shaft. The first of these arrangements was bolted to the cantilever wall support, and is called the cantilever bearing.

### **3.1.5 Tube Bearing**

This bearing was designed to rigidly support the impeller shaft in the center of the tubular tank. This bearing was also constructed to dampen vibrations in the impeller shaft.

### **3.1.6 DC Motor**

After reviewing a number of research papers, it was determined that a motor which could output 0.25 horsepower should be chosen for this set-up. The speed of the motor was

controlled with the use of a d.c. motor controller which could vary the motor speed between 0 and 1725 rpm.

### **3.1.7 Torquemeter**

A torquemeter was used in the mixing station to measure the torque being applied to the impeller shaft. By using the relation that power is equal to torque times impeller speed the power input to the system could be calculated. This value is useful in determining impeller efficiencies.

The torquemeter consisted of slip rings which utilized a series of strain gages. Therefore, a Wheatstone bridge was needed for resistance balancing purposes. Two calibrations were done to "zero" the Wheatstone bridge. The first calibration was a mechanical calibration. In this calibration a constant voltage, from 5 mv to 15 mv, is applied to 1/2 of the bridge. A known torque is then applied to the shaft of the torquemeter and a voltage output from the unenergized half of the bridge is measured. As the applied torque was varied, the voltage output varied, therefore a curve of output voltage vs. torque could be plotted. A straight line using regression was plotted through the various data points. Figure 7 shows the results.

The second calibration was an electrical calibration which was used to zero the torquemeter before each use. This calibration was performed so that the same starting point could be attained everytime torque measurements were needed. In this calibration, a decade box input a resistance of 450,000 ohms to one leg of the Wheatstone bridge. The voltage output from the unenergized half of the Wheatstone bridge was then measured. This output value would then be used as a calibration constant for future torque measurement experiments. In future experiments the researcher could again apply a resistance of 450,000 ohms to one leg of the Wheatstone bridge. The researcher would then vary the voltage input to one half of the Wheatstone bridge until the voltage output from the unenergized half of the bridge matched the electrical calibration constant. In this way the torquemeter would

yield reproducible results.

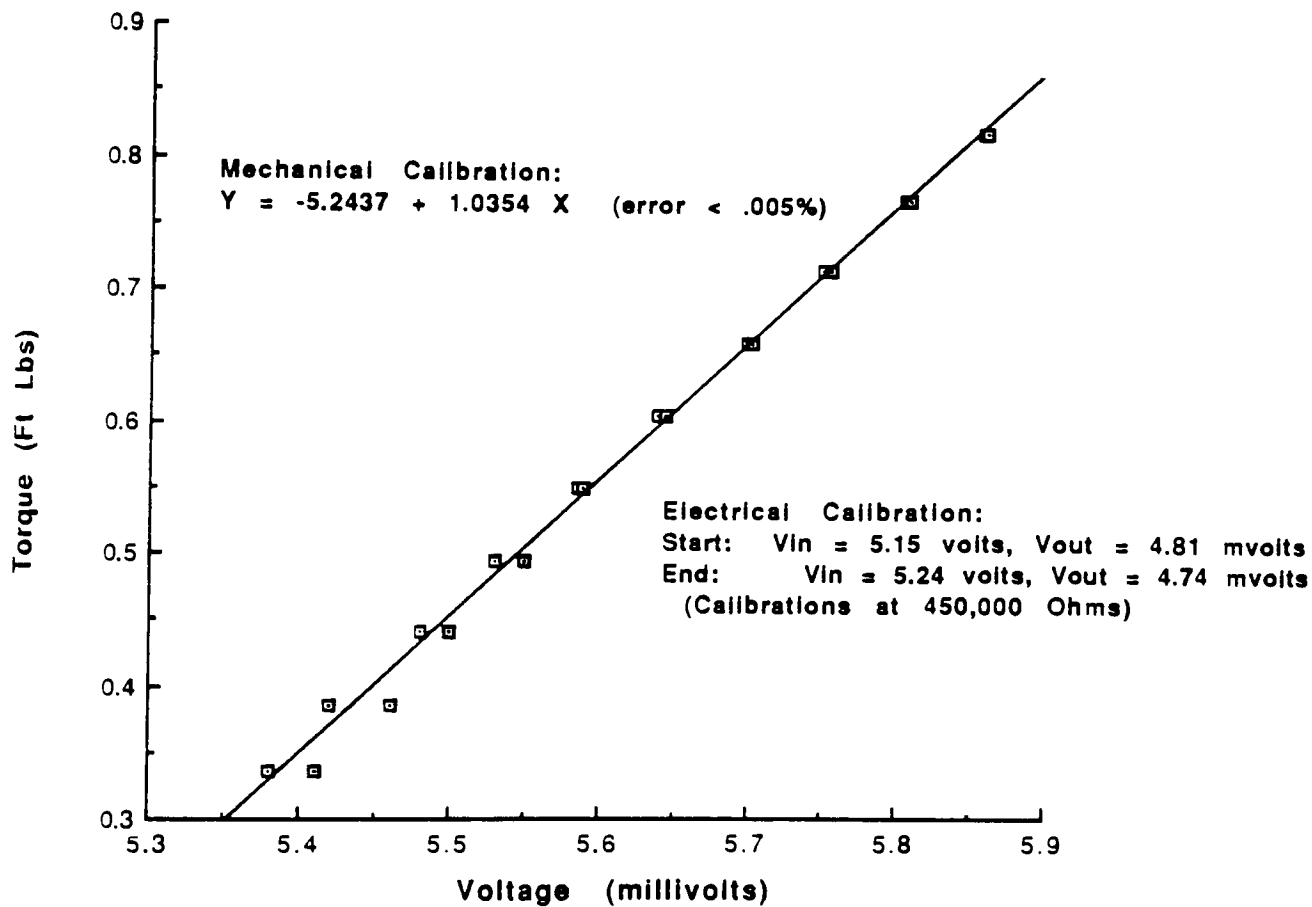


FIGURE 7: Torquemeter Calibration Curve

### 3.2 LASER DOPPLER ANEMOMETER (LDA)

The LDA is well suited for fluid flow studies because it is a non-intrusive measurement tool which can measure positive as well as negative fluid velocities.

The LDA used in this study was operated in the dual-beam mode and consisted of the following components:

- 15 m.W. Spectra Physics He-Ne laser
- Laser Exciter
- Photomultiplier Section
- Photomultiplier Optics
- Beamsplitter
- Beamdisplacer
- Backscatter Section
- Plano-Convex Front Lens
- LDA Counter Module
  - Counter Processor
  - Power Supply
  - D/A Converter Module
  - Data Rate Module
  - Two-Channel LDA Software
- IBM Personal Computer (P.C.)
- P.C. Color Monitor
- Printer

- Three Axis Traverse

An extensive description of the above equipment is given in Appendix B, "Fluid Mixing System Description".

The LDA utilizes the laser to provide incident light which is scattered by moving particles within the mixed fluid. It determines the particle (fluid) velocity from the frequency of the scattered light.

### 3.2.1 The Principle

The LDA measures the frequency difference between the incident light and the scattered light which is known as the Doppler Frequency,  $f_d$ , and can be expressed as:

$$f_d = f_s - f_i = 1/\lambda \vec{V}(\hat{e}_s - \hat{e}_i) \quad (41)$$

where:

- $f_s$  = frequency of scattered light
- $f_i$  = frequency of incident light
- $\hat{e}_s, \hat{e}_i$  = scattered and incident light
- $\lambda$  = incident light wavelength
- $\vec{V}$  = velocity vector
- $\vec{U}$  = velocity component along the x axis
- $\theta$  = angle between the incident and scattered laser beam

By using a monochromatic light source, such as a laser, it is possible to determine  $f_i$  and  $\lambda$ . While, the unit vectors  $\hat{e}_s$  and  $\hat{e}_i$  are dependent upon the system geometry. The velocity vector  $\vec{U}$  measured by the LDA will be in the plane formed by  $\hat{e}_s$  and  $\hat{e}_i$  and perpendicular to a line bisecting the angle between  $\hat{e}_s$  and  $\hat{e}_i$  (see Figure 8).

Since  $\frac{\vec{V}}{\lambda} \cdot (\hat{e}_s - \hat{e}_i) = \frac{\vec{U}}{\lambda} (2 \sin \frac{\theta}{2})$ , Equation (41) can be represented as:

$$f_d = 2 \frac{\vec{U}}{\lambda} \sin \frac{\theta}{2} \quad (42)$$

In terms of U: 
$$\vec{U} = \frac{\lambda f_d}{2 \sin \frac{\theta}{2}} \quad (43)$$

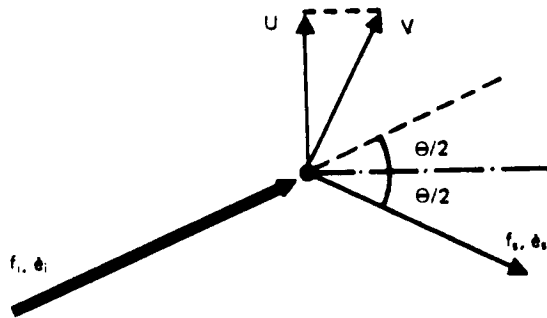


**Figure 8: LDA Velocity Vectors**

The LDA can be arranged in 2 modes of operation. The reference beam mode or the dual-beam mode. The most common mode of operation is the dual beam mode.

### 3.2.2 Dual Beam Mode

The dual beam mode, also known as the differential doppler mode, consists of two laser beams of equal intensity intersecting as shown in Figure 9.

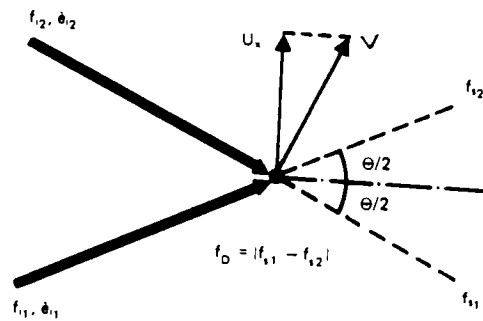


Figure 9 : Dual Beam Mode

$$f_d = |f_{s1} - f_{s2}|$$

The scattered light formed by a particle crossing the intersection volume of the two beams is picked up by the photomultiplier. The Doppler frequency,  $f_d$ , is the difference between the two scattered frequencies,  $f_{s1}$  and  $f_{s2}$ , and is independent of the direction of scatter.

$$f_d = |f_{s1} - f_{s2}| = (\vec{V} \cdot (\hat{e}_s - \hat{e}_i)) / \lambda = 2 \vec{U} / \lambda \sin \theta/2 \quad (44)$$

$$\text{in terms of Velocity: } \vec{U} = f_d \lambda / (2 \sin \theta/2) \quad (45)$$

The dual beam mode can be explained with the use of a fringe model. Here the two coherent and monochromatic laser beams each having plane and parallel wave fronts, interfere in a constructive and a destructive manner to produce a pattern of light and dark interference fringes at the beam crossing (see Figure 10).

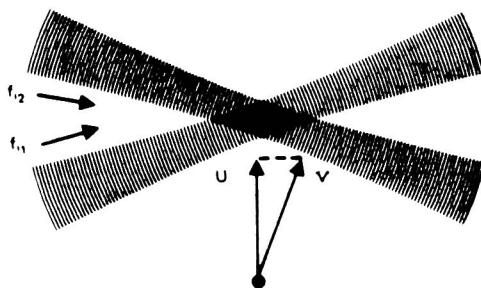


**Figure 10: Fringe Model**

The distance between each consecutive fringe,  $\delta_f$ , can be calculated from the half angle  $\theta/2$  between the two beams and the wavelength of the laser light.

$$\delta_f = \frac{\lambda}{2 \sin \frac{\theta}{2}} \quad (46)$$

As a particle crosses the fringe pattern it scatters light at a rate proportional to its velocity.

$$f_d = \frac{\vec{U}}{\delta_f} = 2 \frac{\vec{U}}{\lambda} \sin \frac{\theta}{2} \quad (47)$$

### 3.2.3 Flow Seeding

The LDA's operation is reliant upon the laser light being scattered by particles within the flow. The quality of the scattered light is therefore dependent upon five major factors:

- Particle (seeding) concentration
- Particle size distribution
- Laser power
- Mode of operation
- Size of particles in relation to fringe spacing

Seeding concentration and size distribution are the most important of the five factors. The seeding concentration should be high, so that the signal received from the signal processor (counter) is nearly continuous; while the size of the particles must be large enough to scatter light, but also small enough to follow the smallest of fluid fluctuations. The seeding diameter is  $.1\mu$  to  $1\mu$  for gases, and  $1\mu$  to  $10\mu$  for liquids. Table 1 lists seeding particles for a variety of applications.

**Table 1**  
**Methods of Seeding**

<b>Flow Medium</b>	<b>Seeding Material</b>
Water	Polystyrene
	Milk
	Latex paint
Air	Water vapor
	Di-octylphthalate (LOOP)
	Teflon dust
	Silicon oil droplets
	Titanium dioxide
	Geon (PVC)
	Aluminum
	Aluminum oxide
	Ammonium chloride
	Stannic chloride
	Tobacco smoke
	Magnesium oxide
	Smoke bombs
	Smoke pellets
	Silicon dioxide
Magnesium oxide	
Silicon oil droplets	

### **3.2.3 Signal Processing**

In order to measure fluid velocity, laser light scattered by fluid particles must be processed by a signal processor. In this study, a counter processor was used. The counter acts like an electronic stopwatch which measures the time it takes for a particle to cross a known number of light fringes. The counter is very useful when using fluids which have low seeding concentrations, because it can operate on intermittent signals. Each seeding particle processed by the counter contributes statistically to mean and fluctuating velocity calculations.

## **3.3 EXPERIMENTAL PROCEDURE**

### **3.3.1 Typical Experimental Procedure**

- Inspect the set-up for mechanical and electrical integrity.
- Fill tubular and cubical tanks with deionized water.
- Cover both tanks to keep the system free from dust, while at the same time allowing the tanks the ability to breathe. If data is taken with bubbles coalescent on the tank walls, false velocity values will be recognized.
- Measure the water temperature in the tubular tank, in order to determine the water's density and viscosity.
- Install the impeller, impeller shaft, and the tubular tank steady bearing.
- Add 4 to 5 drops of polystyrene seed particle solution to the tubular tank fluid. The seeding particles will be experimentally useful for four to five days.
- Set the motor controller to the desired approximate rpm setting. The controller is incremented in ten equal divisions, with each division representing a 190 rpm increase over the previous division.
- Calculate the shaft rpm by using the B & K 4913 digital stroboscope.

- The system torquemeter was designed to operate between 0 in-lb<sub>f</sub> and 10,000 in-lb<sub>f</sub>. The torque measured was estimated to be between 5 and 10 in-lb<sub>f</sub>'s. The torquemeter was therefore measuring a very small percentage of its capability. Consequently, a very noisy and inaccurate signal was realized.
- As an alternative, measurements of electrical power draw were taken. An HP digital multi-meter was used to measure the system current and voltage draw, so that power draw could be calculated.
  - Current is measured by placing the multi-meter in series with the 1/4 horsepower motor power line, while voltage is measured by placing the multi-meter in parallel with the 1/4 horsepower motor power line.
  - Experimental values are taken at the beginning as well as at the end of each run. The data is then averaged, and a mean power draw value is calculated.
- The laser is powered up so that it can attain a "warmed up" state by the time experimental measurements are to occur.
- The system oscilloscope, counter, and PC and printer are also powered up.
- Start the dc motor at the desired rpm setting.
- Utilize the oscilloscope to monitor the Doppler bursts being received via the photomultiplier.

### **3.3.2 Counter Settings**

- Use the amplifier gain settings on the counter to amplify or to attenuate the data rate. The optimum operational data rate is .1 kHz.
- Set the threshold window to its broadest band, so that all the data signals can be evaluated.
- Set the system accuracy to 6%. By setting the accuracy to a higher value the system sampling time may expire before the minimum number of data points are collected.

- Adjust the DAC gain settings to amplify the data rate and % validation values, noting that data rates of .1 kHz and that % validation values over 10% are acceptable. If the DAC gain overload light is illuminated, the gain must be attenuated.
- Data is collected and the histogram of the data is viewed by using the LDA software "HISTO" function. By reviewing the histogram, high pass and low pass filters can be used to filter data which appears erroneous.
- The voltage adjust value for the photomultiplier is set between 1.5 kV and 1.75 kV, while the photomultiplier current is set at 25 micro amps.
- The application of additional seeding material is used to tailor the data rate and % validation signals. Additional seeding will raise the data rate while it lowers the % validation value.

### 3.3.3 LDA Software Program

- To enter the LDA program mode, **LDA2D** is typed and the enter key is depressed.
- **CAPS LOCK** and color mode operation is selected.
- The LDA menu screen has now been accessed. By utilizing the arrow keys on the PC, the various menu code options can be selected. The menu screens are self-explanatory and a tutorial is available.
- The arrow keys are used to select **PARAMETERS** and the enter key is depressed. At this point the system parameters are selected.
- Once the system parameters are set, the profile mode is entered by arrow keying to **PROFILE** and depressing the enter key. Once in the profile mode the profile buffer is reset by arrow keying to **NEW**, and depressing the enter key.
- The traverse parameters are manually entered, after arrow keying to **TRAVERSE**, and depressing the enter key.

- The system has been initialized and is ready to take one run of data points.
- Data collection is implemented by arrow keying to the **COLLECT** option and depressing the enter key. The system will now begin to acquire data. The maximum sampling time the system will use is 1,000 seconds per channel. If the maximum sampling time expires, the system will abort the data collection process. Under normal operating conditions the maximum sampling time does not expire. Times at which expiration may occur are during measurement of very low velocity values.
- Once data has been collected for the first traverse point the data can be **LISTED**, **MOMENTED**, or **HISTOGRAMED**. At this point the profile buffer will contain 1 point.
- New traverse parameters are again set with the manual traverse. At this point a second data collection is implemented. Again the data can be **LISTED**, **MOMENTED**, or **HISTOGRAMED**. The profile buffer will now contain 2 points.
- The above process is repeated until a complete velocity profile has been processed. When the velocity profile is completed, the **SAVE** option is arrow keyed and the enter key is depressed. This first velocity profile will be saved under the name **RESULT.LST**. This profile can be viewed or printed by using the appropriate menu code options.
- After each experimental run the file **RESULT.LST** should be renamed to a file which categorizes the collected data. If the **RESULT.LST** file is not renamed it will be lost when the next velocity profile is completed.

The previously described data collection procedure was used during forty eight experimental runs. The experimental runs are listed in Appendix D, under the heading Experimental Velocity Profiles.

## **4.0 RESULTS AND DISCUSSION**

The results contained in this section are presented in graphical and tabular form. Velocity profiles, pumping capacities, and power consumption rates as functions of impeller speed and position are given.

### **4.1 Axial Velocity Profiles**

#### **4.1.1 Velocity Profiles at Fixed Positions**

Since an axial impeller is designed to generate mostly an axial flow as opposed to a radial flow, the axial profiles generated by an axial impeller are more descriptive than their radial profiles. Therefore, only the axial profiles generated by the axial impeller are shown in this section.

The axial velocity profile measurements were made at 0.635, 1.27, and 2.54 cm above the tip of the impeller and at impeller speeds of 3.33, 5.0, 8.33, and 11.66 rps. Figures 11, 12, and 13 illustrate these axial velocity profiles.

Figures 14, 15, and 16 reveal velocity vectors at various axial positions within three separate set-ups. When these figures are compared to Figures 11, 12, and 13 it can be seen that the experimental data behaves similarly to that found by the referenced workers.

An axial impeller induced flow pattern for a .406m diameter impeller operating in a baffled circular cylinder is shown in Figure 15. Comparing this figure to Figures 11, 12, and 13 shows that the experimental set-up behaves similarly to the referenced works.

Axial velocity vectors for a 16" axial impeller operating in a 48" diameter tank are shown in Figure 16, and can be compared to Figures 11, 12, and 13. The data has been collected with the use of a Laser Doppler Velocimeter (LDV) which illustrates that the fluid motion is directed toward the base of the tank. The flow then moves along the base and up the side walls.

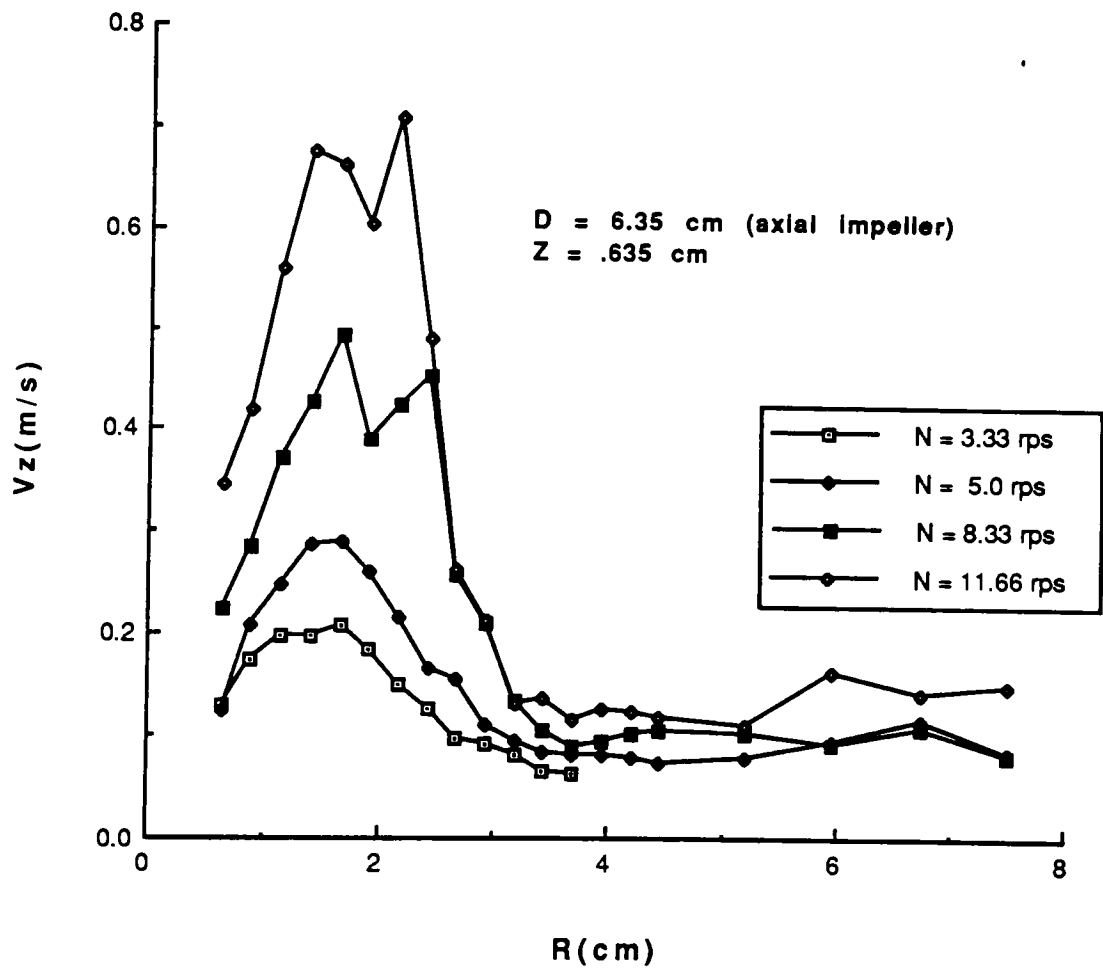


Figure 11: Axial Velocity Profiles (Runs for Jun5 at Q)

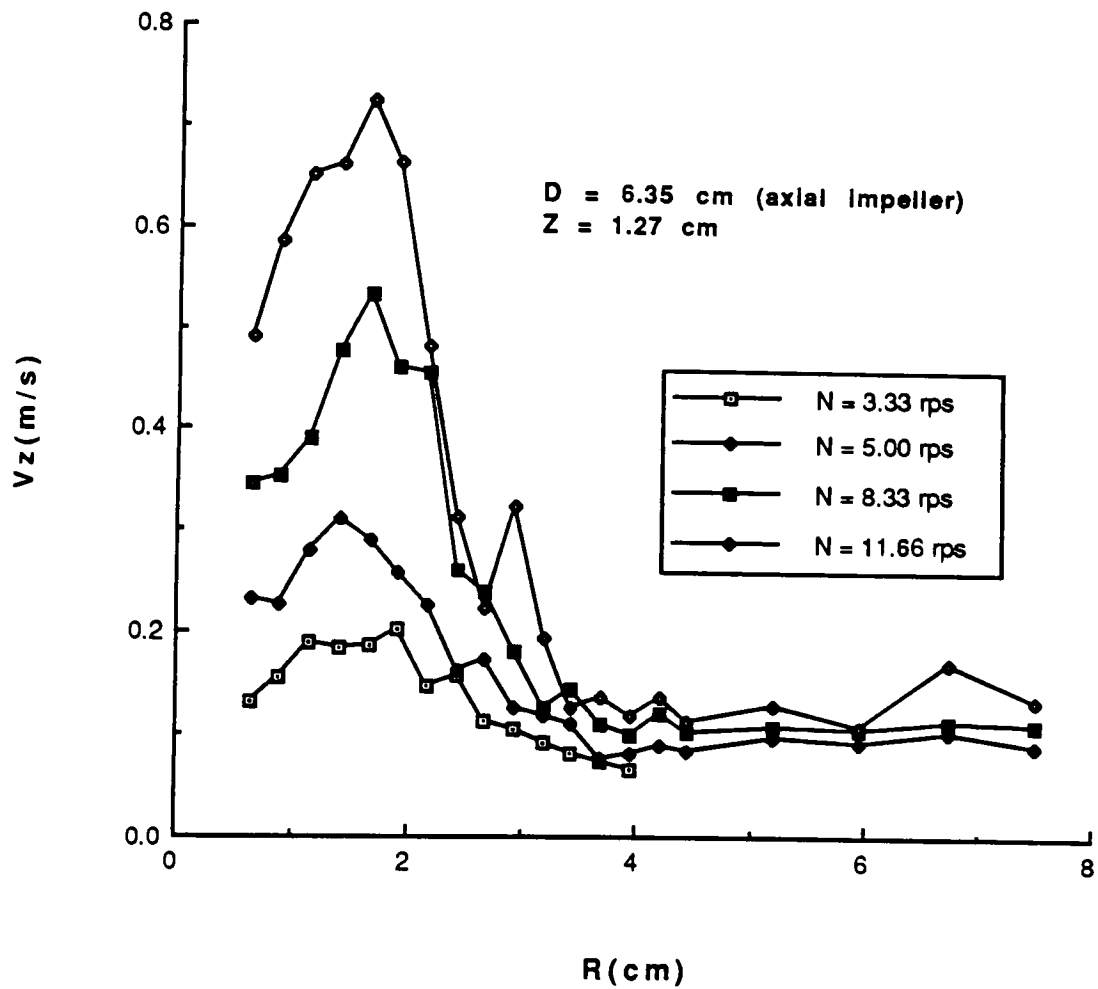
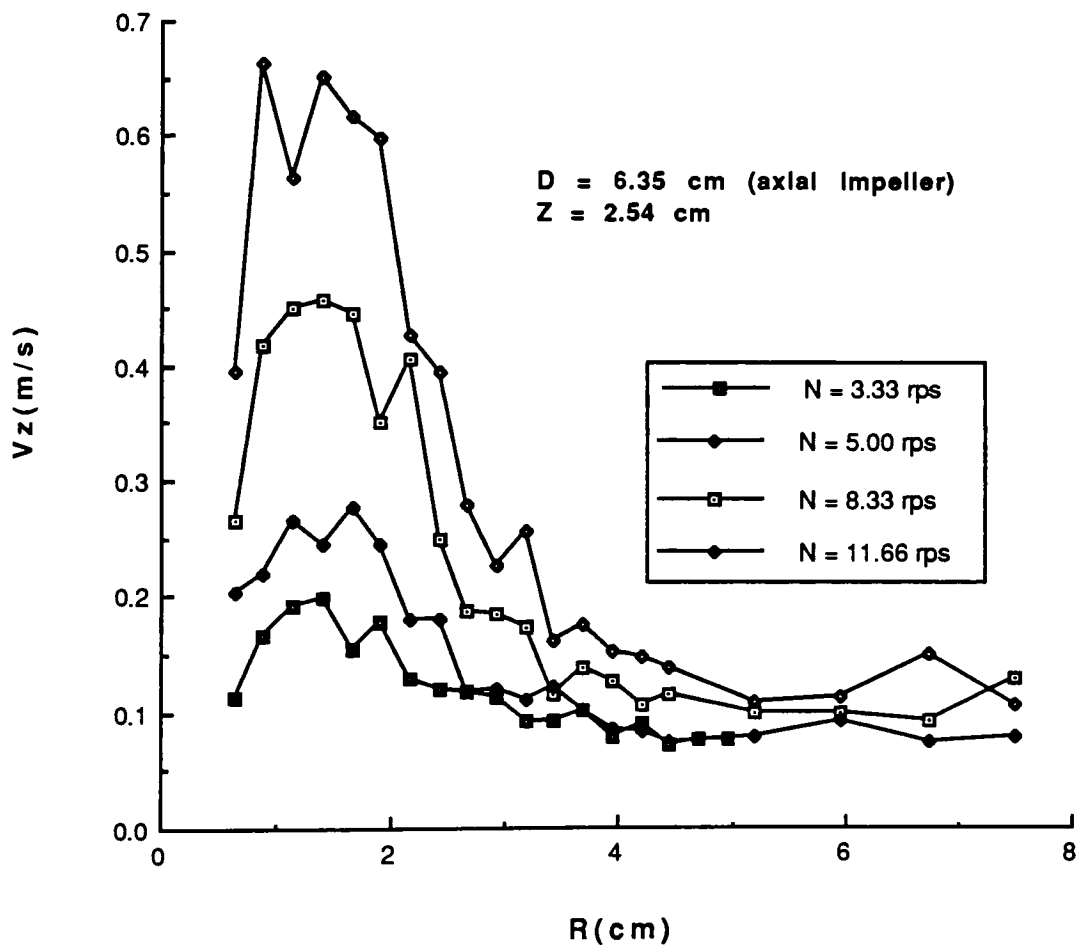


Figure 12: Axial Velocity Profiles (Runs for Jun5 at H)



**Figure 13: Axial Velocity Profiles (Runs for Jun5 at O)**

**MEAN VELOCITY VECTORS IN R-Z PLANE  
RUN 7.19.85.5**

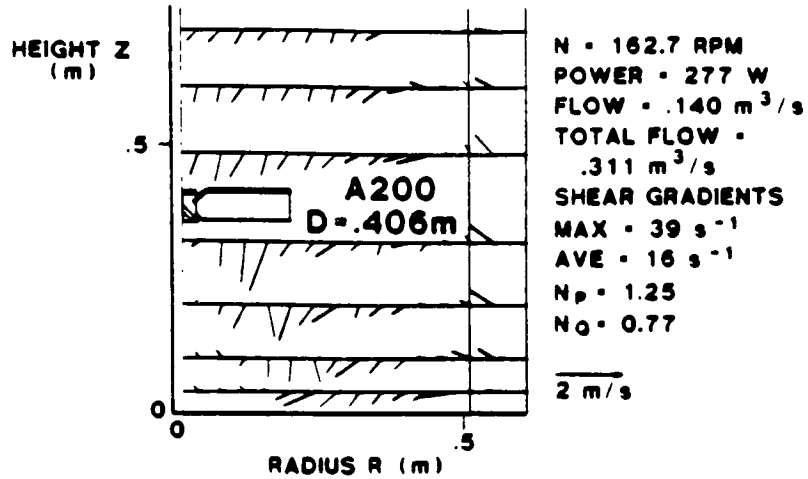


Figure 14: Axial Velocity Profiles as Reported by Weetman & Oldshue(21)

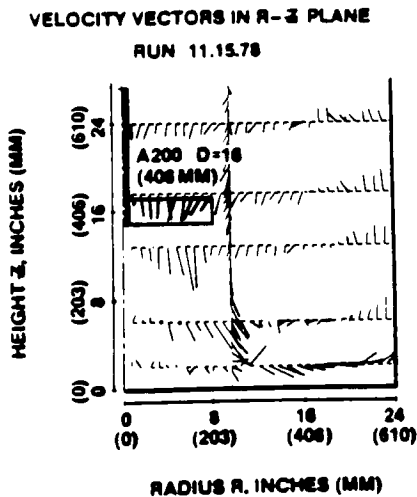
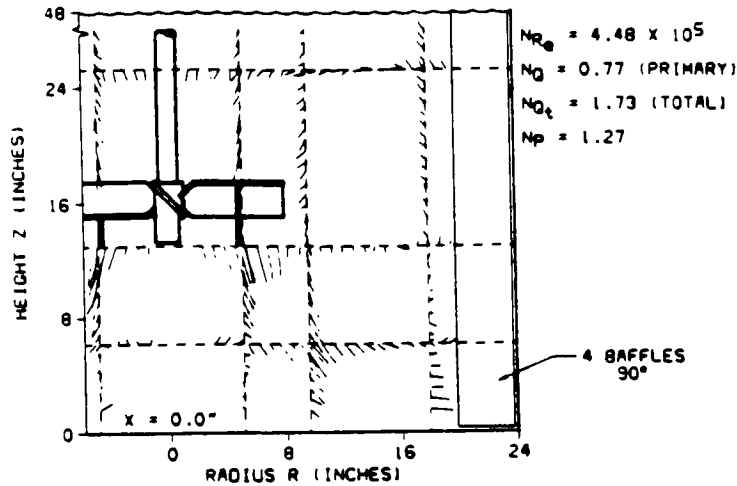


Figure 15: Axial Velocity Profiles as Reported by Weetman & Salzman (20)



**Figure 16: Velocity Vectors in the R-Z Plane, Oldshue(13)**

Examination of these Figure 11, 12, and 13 reveals three interesting characteristics:

- 1) In all three cases the flow induced by the impeller is characteristic of the axial flow generated by a top to bottom axial impeller (See Figure 2).
- 2) Experimental findings of Weetman & Oldshue (21), Weetman & Salzman (20), and Oldshue (14) as shown in Figures 14, 15, and 16 respectively, corroborate the findings illustrated in Figures 11, 12, and 13. The profiles shown in Figures 11, 12, and 13 are represented in an inverse configuration to those found by the referenced works. This inverse relationship is due to the fact that the impeller used in this study was a top to bottom axial flow impeller; while the impellers used in the referenced works were bottom to top configured axial impellers.
- 3) As the speed of the impeller increases the mean impeller velocity also increases, thus generating velocity profiles of greater breadth and magnitude.

Missing Page

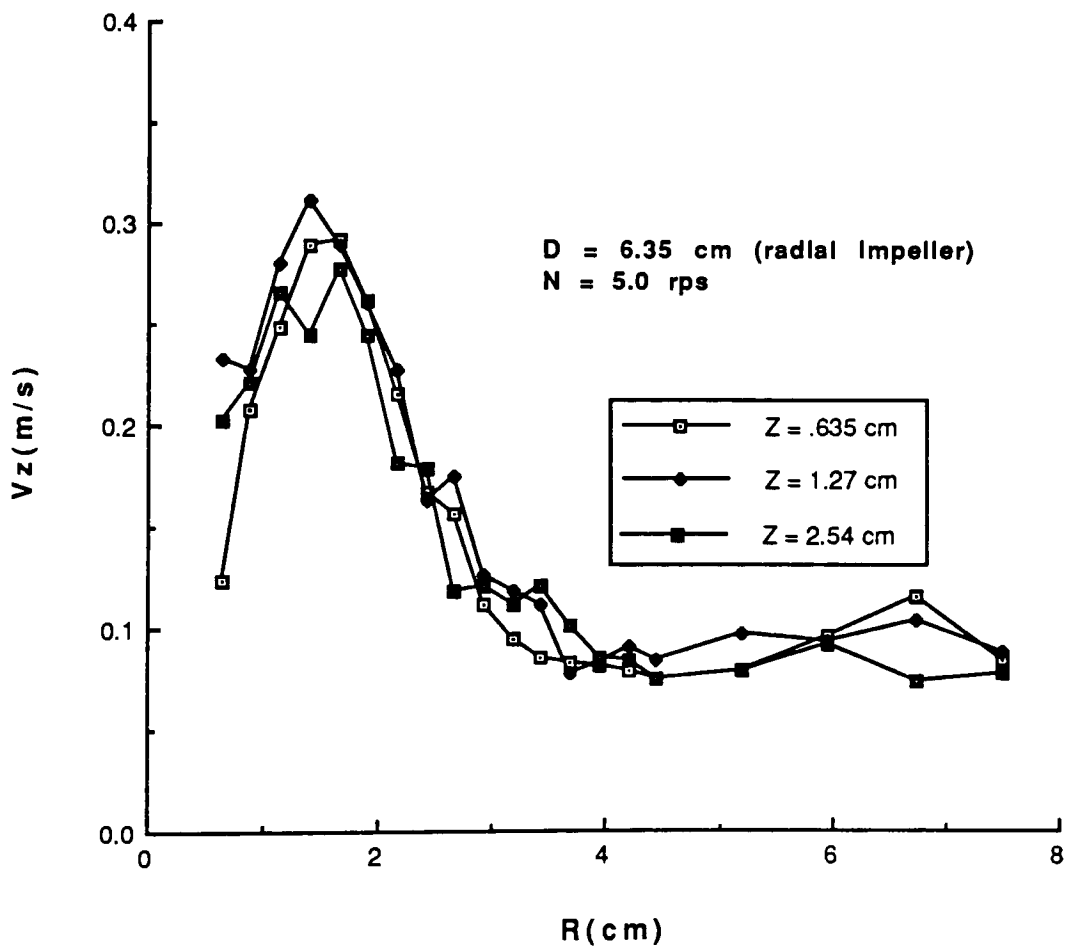


**Figure 18: Axial Velocity Profiles (Jun53ax runs)**

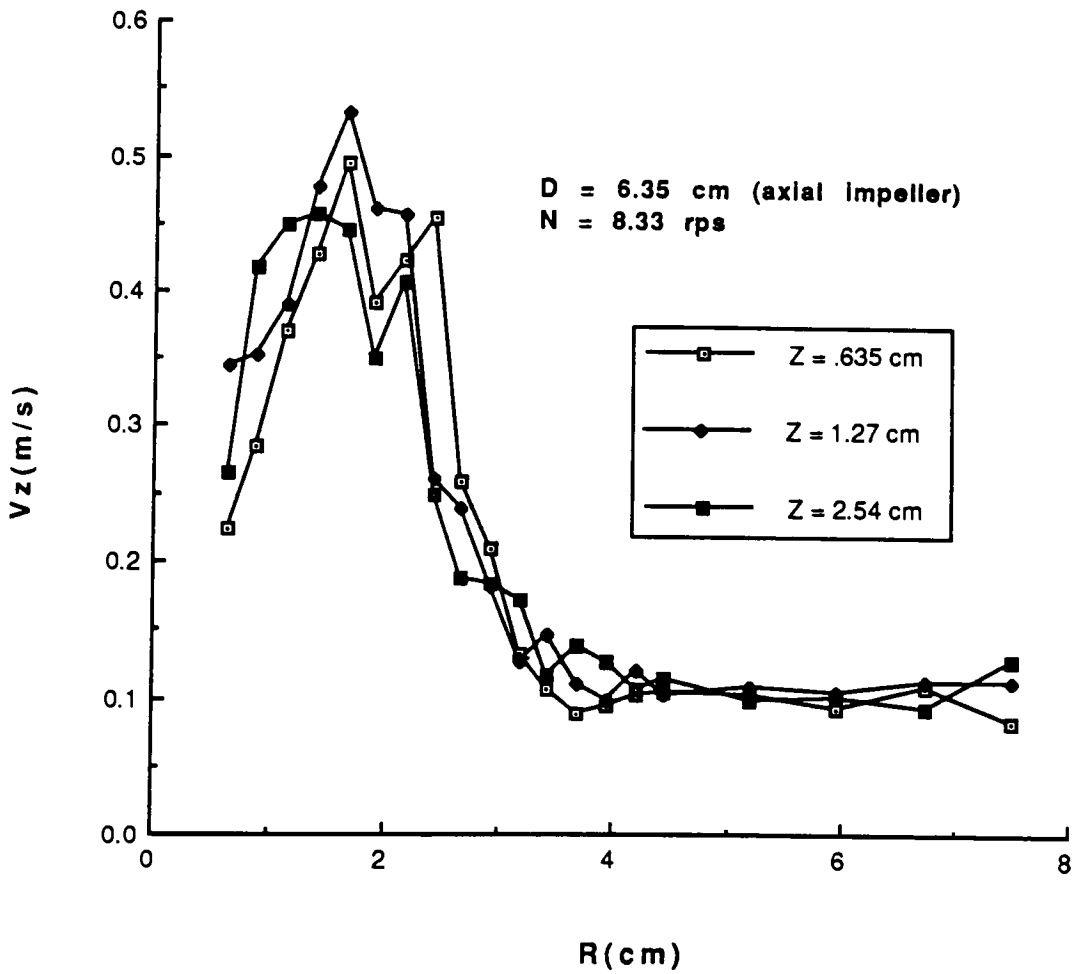
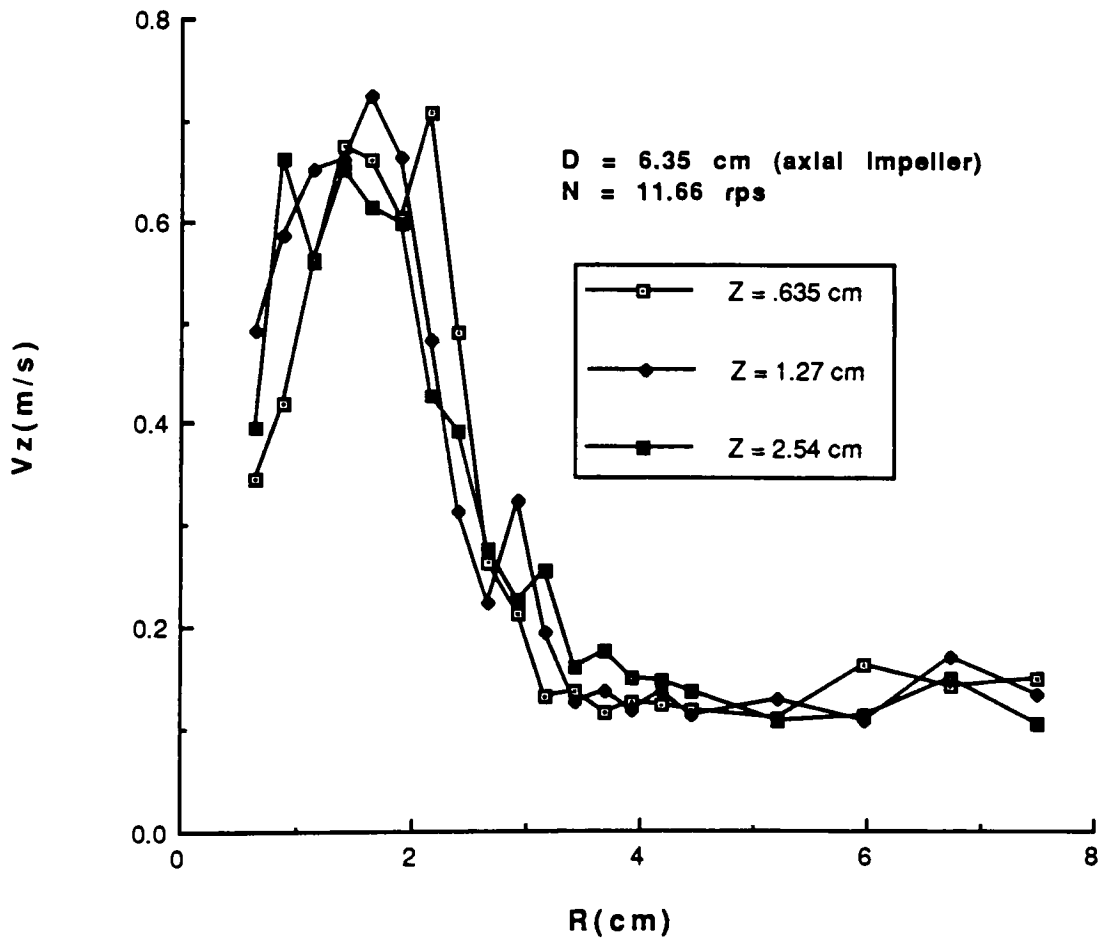


Figure 19: Axial Velocity Profiles (Jun55ax runs)



**Figure 20: Axial Velocity Profiles (Jun57ax runs)**

Figures 17, 18, 19, and 20 reveal that at fixed impeller speeds, the measuring position above the impeller does not have an appreciable affect upon the resulting velocity profile. Theoretically, as the measuring point is moved further from the impeller, the velocity profile will become broader and flatter because of viscous fluid and momentum transfer effects. Surprisingly, Figures 17 thru 20 do not exemplify this effect. Possibly the fluid which makes up each profile is characterized by fluid particles which have both positive and negative velocity values which are not discernable by this LDA. If a frequency shifter were employed the negative and positive particle velocity values would be discernable and the profiles might characterize the viscous fluid and momentum transfer effect.

Figures 17 thru 20 all reveal that the point of maximum velocity occurs at  $R = 0.65$  cm. This maximum velocity profile position is due to the design of the axial flow impeller. At 0.65 cm radially outward from the center of the impeller, the blades abruptly twist downward. This abrupt design change in the impeller generates the point of maximum velocity.

## **4.2 Radial Velocity Profiles**

### **4.2.1 Velocity Profiles at Fixed Positions**

Radial velocity measurements at .635, 1.27, and 2.54 cm beyond the tip of the radial impeller were generated for all the impeller speeds studied. Figures 21, 22, and 23 illustrate the four velocity profiles generated at impeller speeds of 3.33, 5.0, 8.33, and 11.66 rps's.

The flow patterns shown in Figures 21, 22, and 23 are characteristic of the radial flow induced by a typical radial flow impeller. Experimental findings of Oldshue (12), as shown in Figure 24 corroborate the findings of this work.

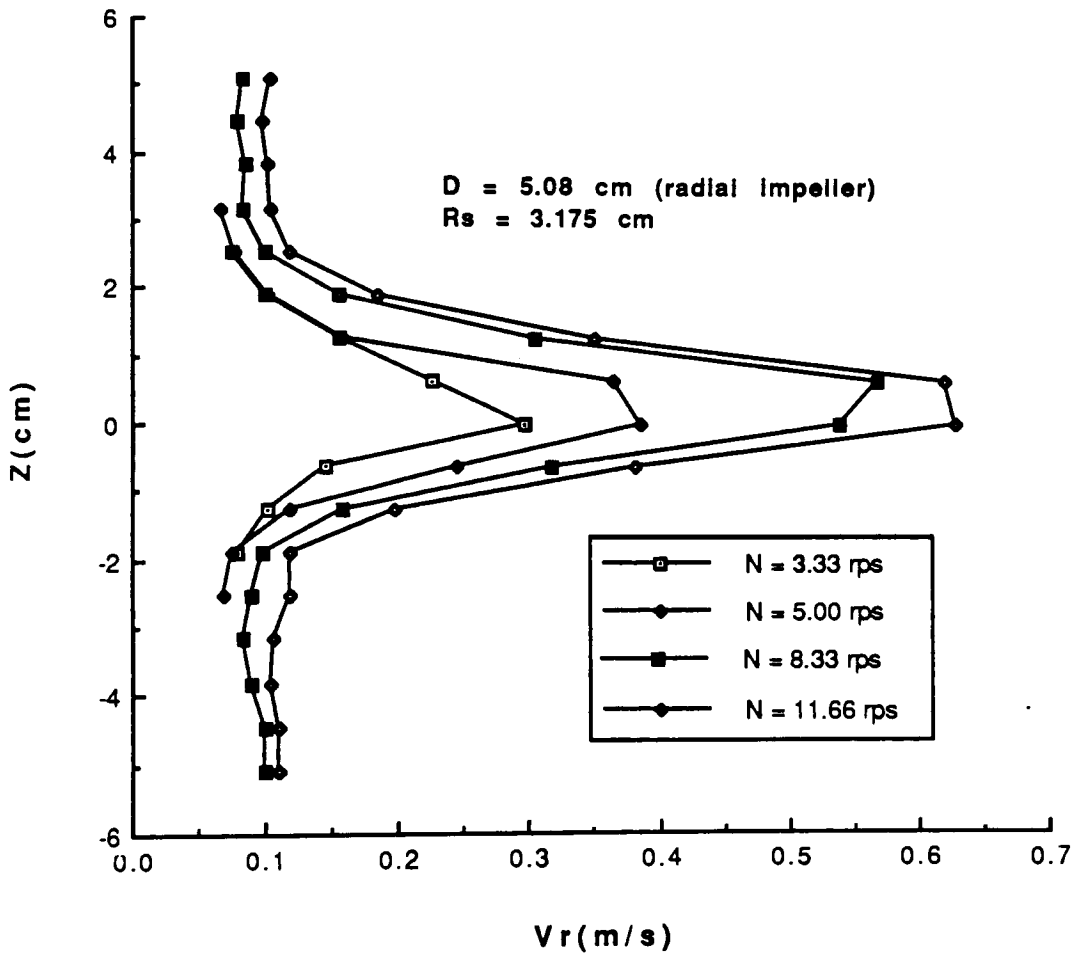
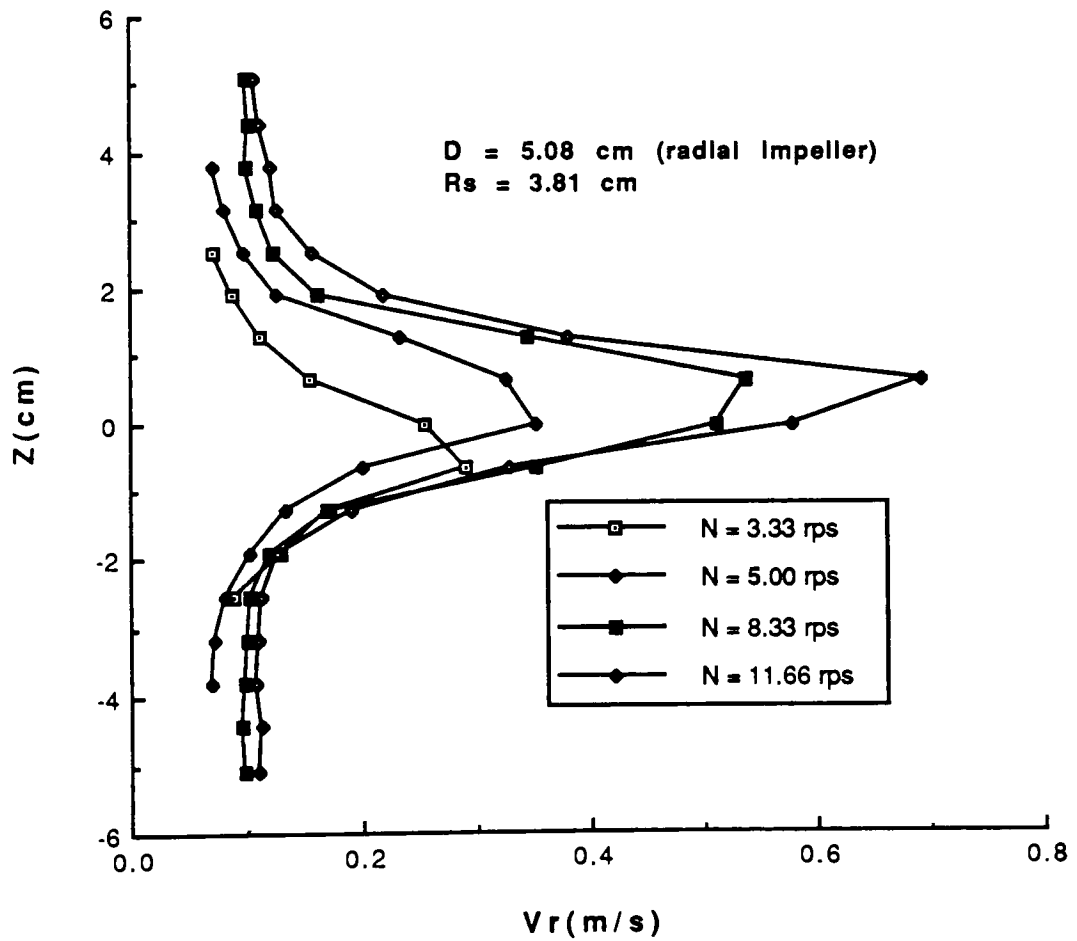
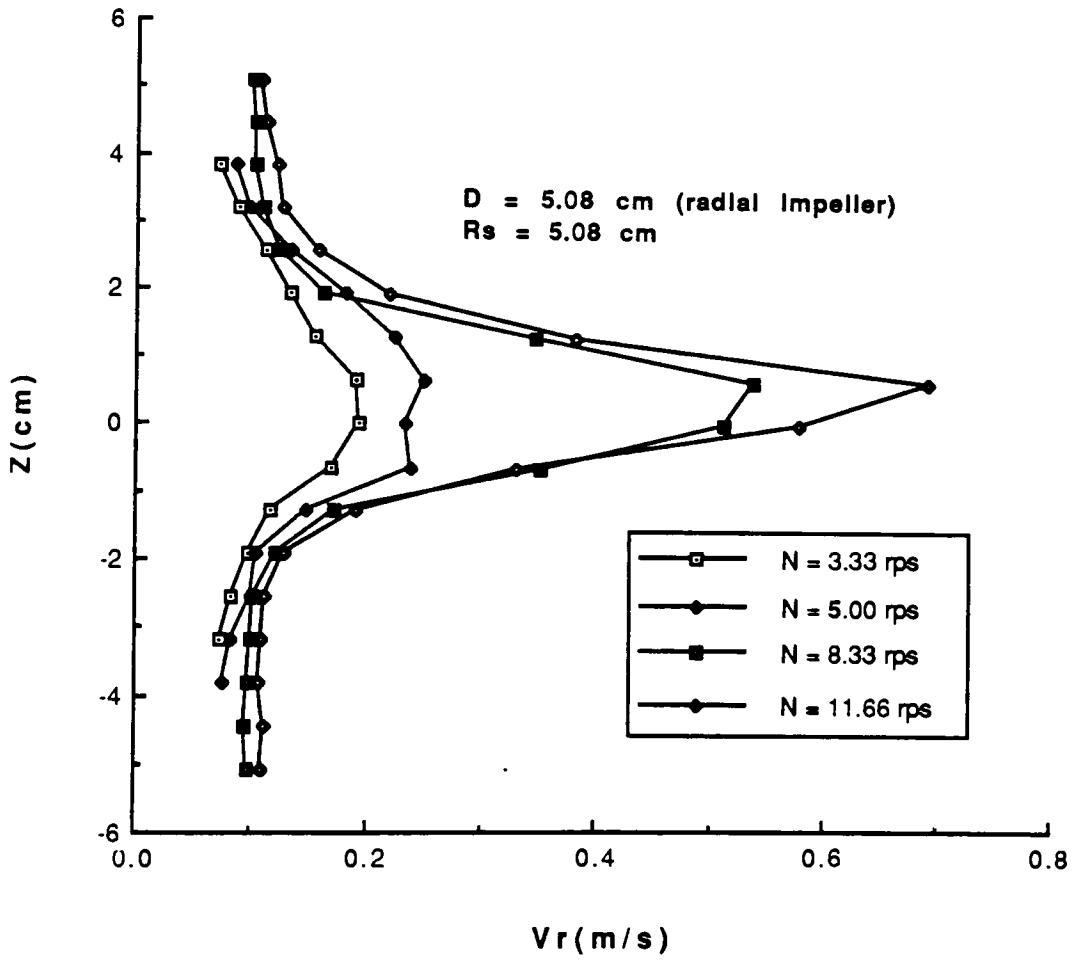


Figure 21: Radial Velocity Profiles (Runs for Jun7 at Q)



**Figure 22: Radial Velocity Profiles (Runs for Jun7 at H)**



**Figure 23: Radial Velocity Profiles (Runs for Jun7 at O)**

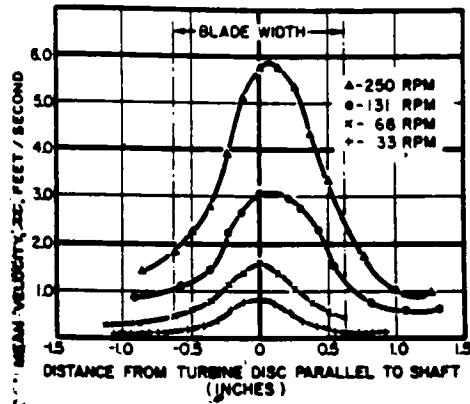


**Figure 24: Radial Velocity Profiles as a Function of Impeller Speed, Oldshue(12)**

#### **4.2.2 Velocity Profiles at Fixed Impeller Speeds**

Radial velocity profiles at constant impeller speeds and at different radial positions were studied. Figures 25, 26, 27, and 28 are taken at impeller speeds of 3.33, 5.0, 8.33, and 11.66 rps respectively. Each of the three profiles on each of the four figures illustrate how measuring volume position effects the resulting velocity profile.

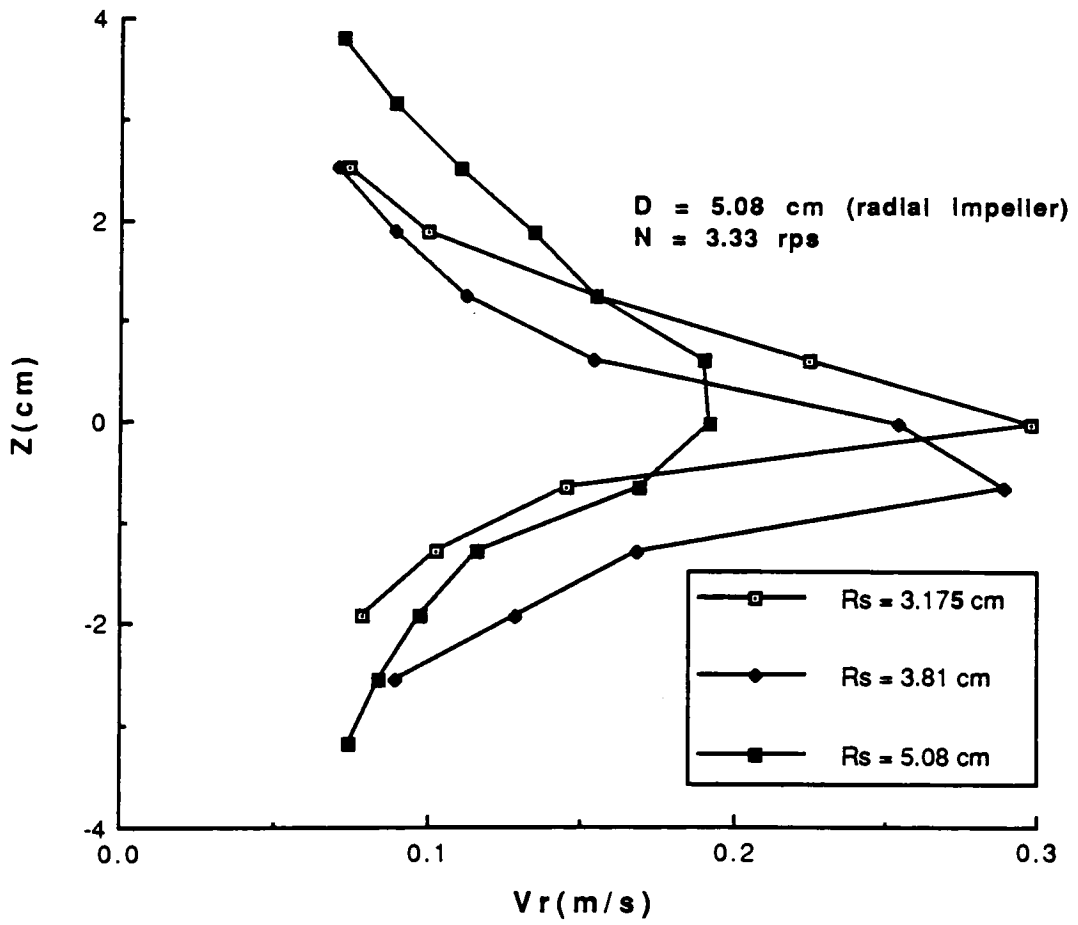


Figure 25: Radial Velocity Profiles (Jun 72 runs)

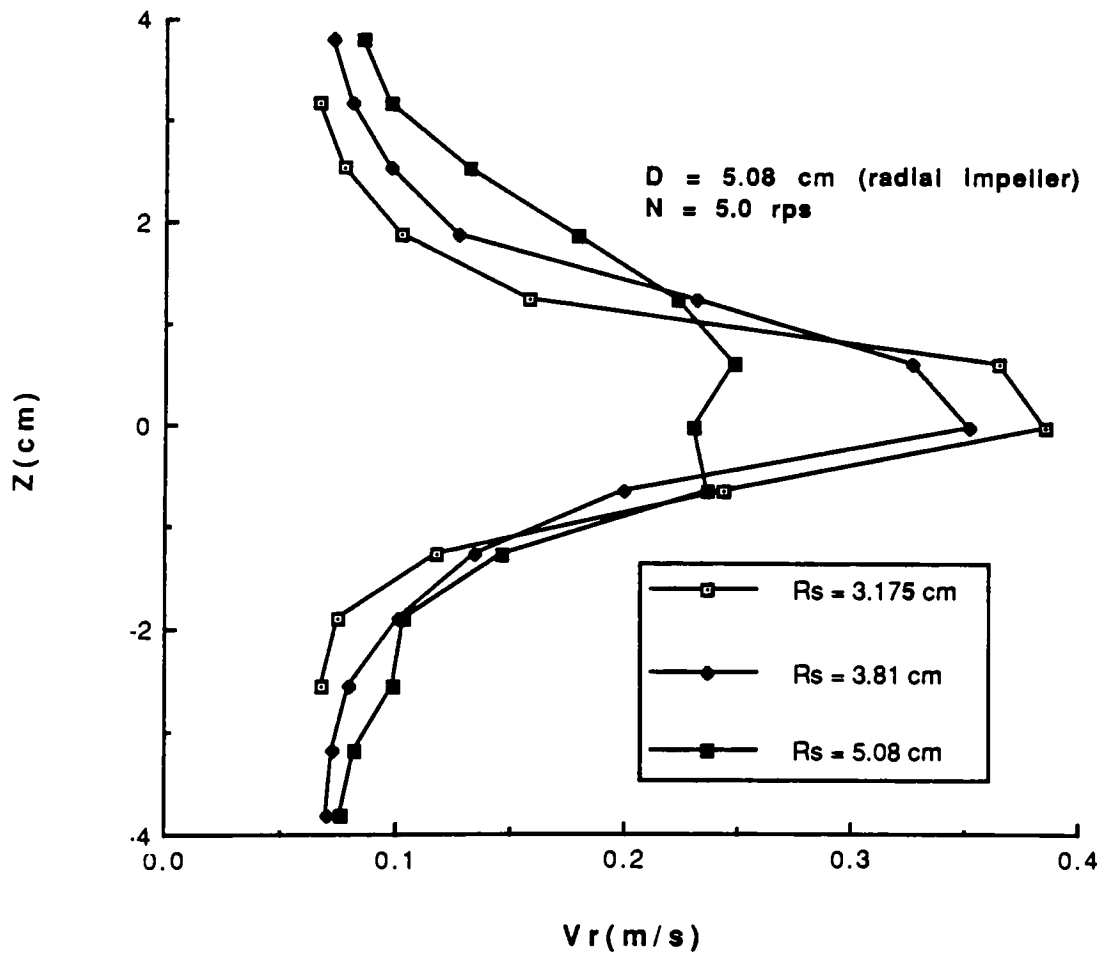


Figure 26: Radial Velocity Profiles (Jun 73 runs)

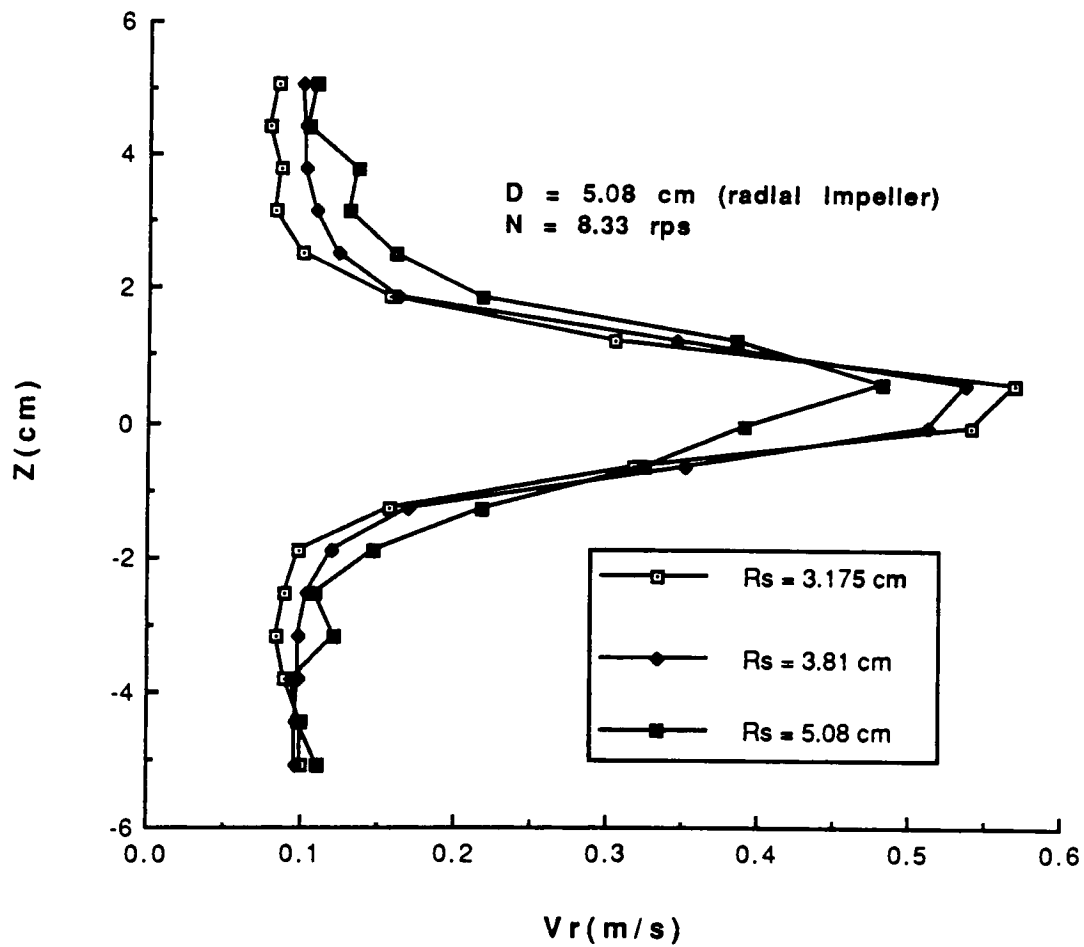
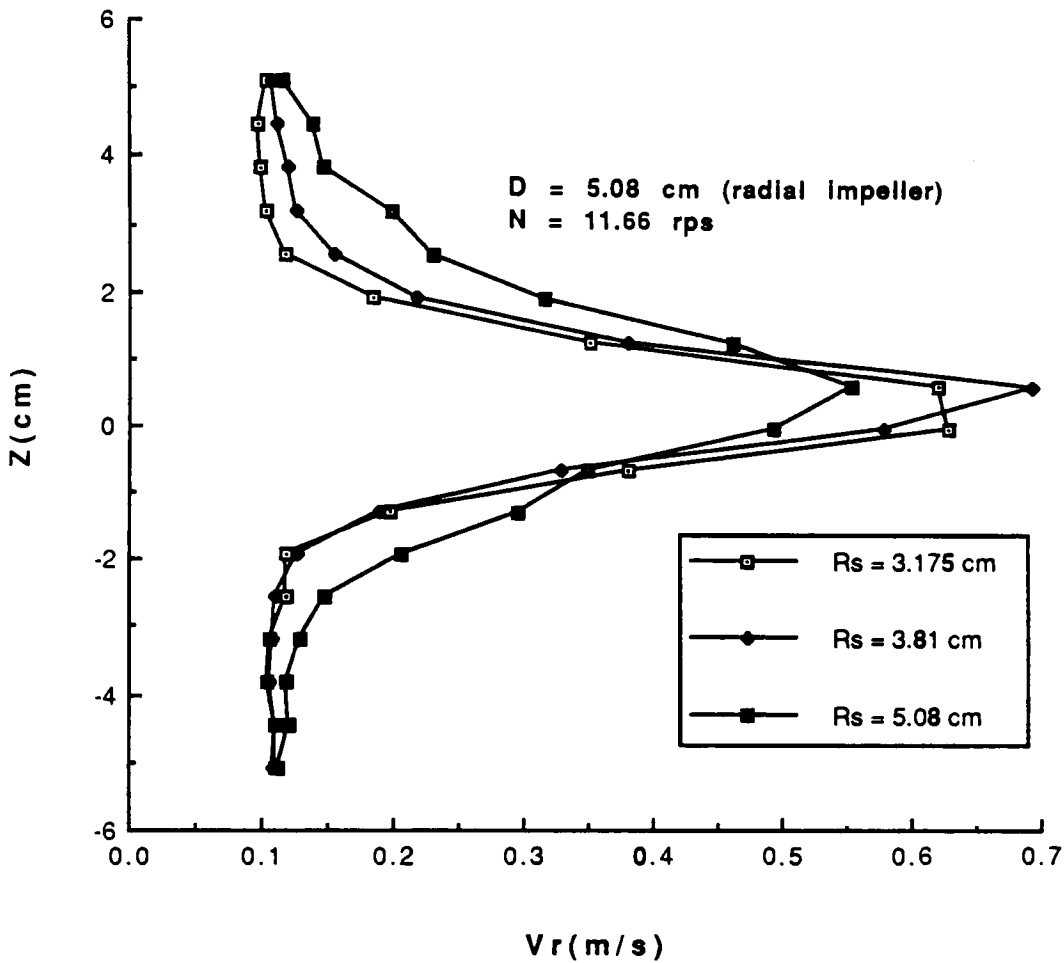


Figure 27: Radial Velocity Profile (Jun75 runs)



**Figure 28: Radial Velocity Profiles (Jun77 runs)**

As the measuring point is moved further from the tip of the impeller, the velocity profile will become broader and flatter because of viscous fluid and momentum transfer effects, as illustrated in Figures 25 thru 28. Figure 29 by Cooper and Wolf (3) and Figure 30 by Weetman and Salzman (20) corroborate these findings.

The deterioration of radial velocity profiles at increasing radial distances from the tip of a six blade impeller is shown in Figure 29.

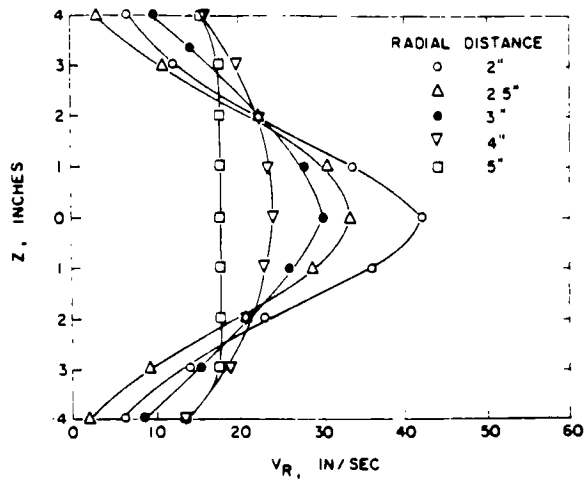


**Figure 29 Radial Profile Deterioration as a Function of  $R_s$ , Cooper & Wolf(3)**

The radial velocity vectors as generated by a .406 m Rushton turbine are also shown in Figure 30. The magnitude and direction of the velocity vectors were measured using a laser velocimeter.

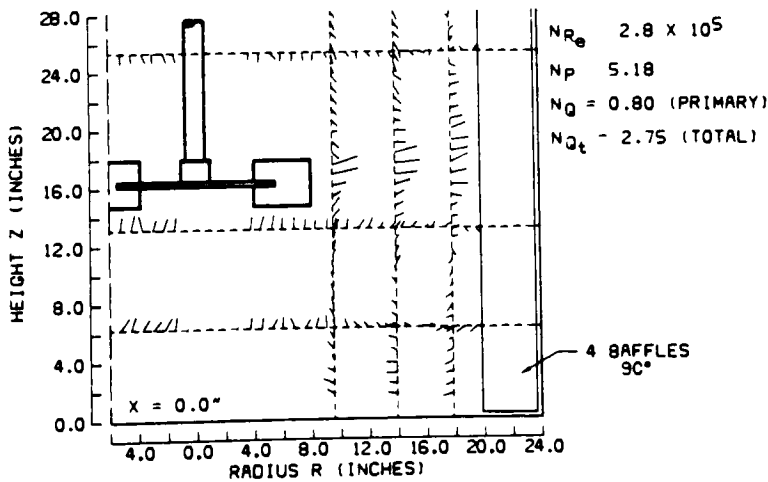


**Figure 30: Radial Velocity Profiles Generated by a Rushton Turbine Weetman & Salzman(20)**

In looking at Figures 21 thru 23 and 25 thru 28 it is apparent that due to the symmetry of the radial impeller, that the profile maximum velocity point emanates from the midpoint of the impeller.

#### 4.1.4 Axial and Radial Tip Velocities vs. Maximum Fluid Velocity Comparison

When operating a mixing system it would be beneficial to operate the impeller at a speed most efficient for transferring the largest percentage of the tip velocity to the fluid flow. In this way most of the mechanical energy contained in the rotating impeller would be used for mixing purposes. Shown below in Table 2 is the comparison of tip velocities to maximum profile velocities.

**TABLE 2**

**Impeller Tip Speed Comparison to Maximum Fluid Velocity**

**IMPELLER SPEEDS**

3.33 rps	5.0 rps	8.33 rps	11.66 rps
----------	---------	----------	-----------

**AXIAL TIP VELOCITIES BASED UPON THE FOUR IMPELLER SPEEDS**

0.2979 m/s	0.3861 m/s	0.5686 m/s	0.63 m/s
------------	------------	------------	----------

**ABSOLUTE MAXIMUM FLUID VELOCITY VALUES**

0.169 m/s	0.254 m/s	0.423 m/s	0.592 m/s
-----------	-----------	-----------	-----------

**% OF TIP VELOCITY TRANSFERRED TO FLUID FLOW**

56%	66 %	74%	94%
-----	------	-----	-----

**RADIAL TIP VELOCITIES BASED UPON THE FOUR IMPELLER SPEEDS**

0.346 m/s	0.519 m/s	0.864 m/s	1.176 m/s
-----------	-----------	-----------	-----------

**ABSOLUTE MAXIMUM FLUID VELOCITY VALUES**

0.209 m/s	0.312 m/s	0.533 m/s	0.726 m/s
-----------	-----------	-----------	-----------

**% OF TIP VELOCITY TRANSFERRED TO FLUID FLOW**

60.3%	60.2%	61.6%	61.7%
-------	-------	-------	-------

In reviewing the above table it is apparent that at higher speeds most of the axial impeller tip velocity is transferred to the fluid flow; while at all speeds the rate of radial velocity transference is relatively constant.

## 4.2 PUMPING CAPACITIES

One of the primary goals of this project was to study how operating conditions affect impeller pumping rates. Therefore, pumping capacities were calculated at different distances from the impellers and at different impeller speeds.

### 4.2.1 Axial Pumping Capacity

Axial pumping capacities have traditionally been calculated over the length of the impeller blade. The following section provides pumping rate information calculated for a control volume over the length of the impeller blade, and also over a broader range. The broader range was studied to see how the pumping capacity changed as the measuring point was moved radially outward from the tip of the impeller. As a result momentum transfer phenomena was witnessed. Figure 31 shows the two scenarios under study.



**Figure 31: Axial Pumping Capacity Area's of Study**

Axial pumping capacity over the length of the impeller blade is illustrated in Figure 32; while Figure 33 illustrates the axial pumping rate over the broader range study. In Figure 33 the pumping rate was analyzed as long as successive mean velocity values changed. The pumping rate was no longer analyzed when subsequent velocity values remained constant. The range of measurements in Figure 32 was from 0 to 3.175 centimeters, while the distance in Figure 33 was from 0 to 3.68 centimeters. This fact implies that an axial impeller is good at generating fluid motion only over the blade length, and it is poor at generating fluid motion at any appreciable radial distance from the tip of the impeller blade.

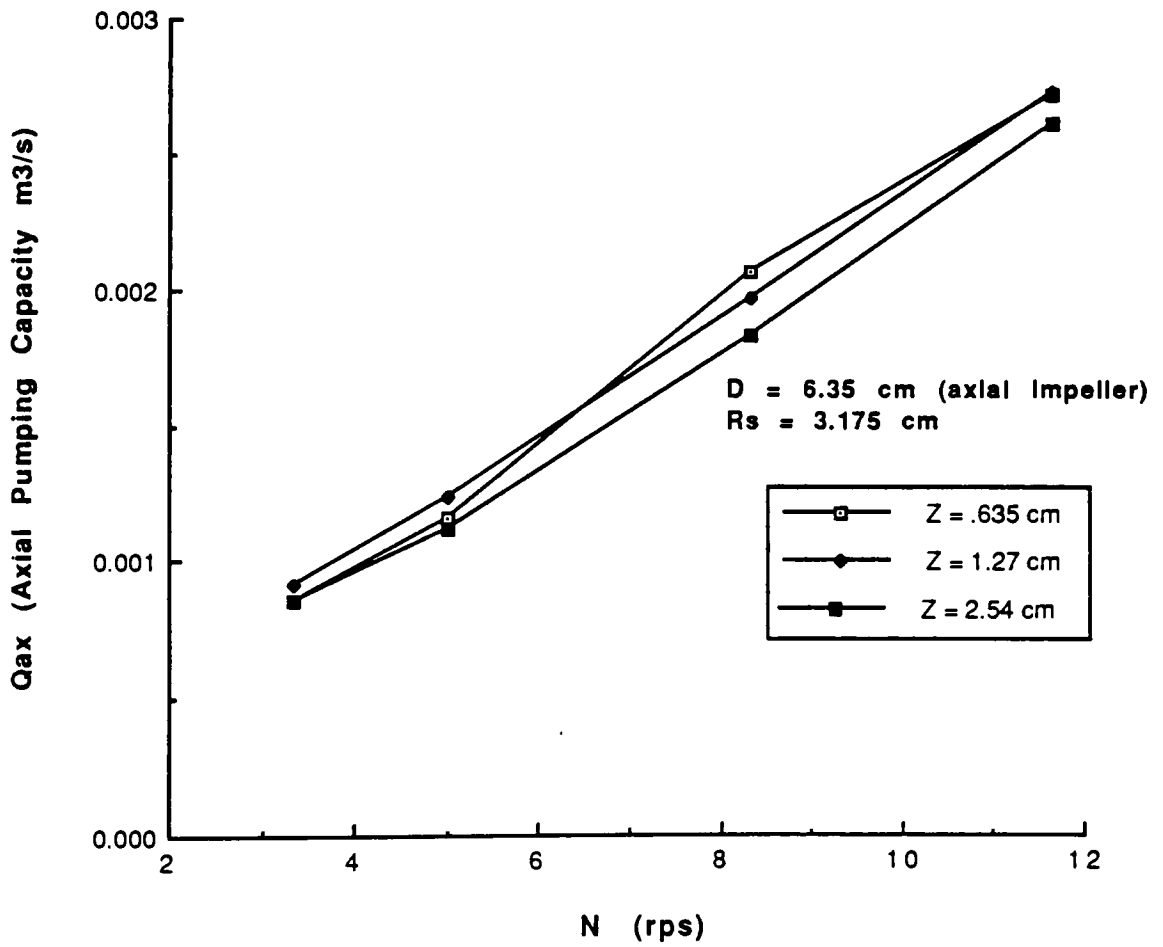


**Figure 32: Axial Pumping Capacity vs. Impeller Speed**  
**Distance = Impeller Blade Length**

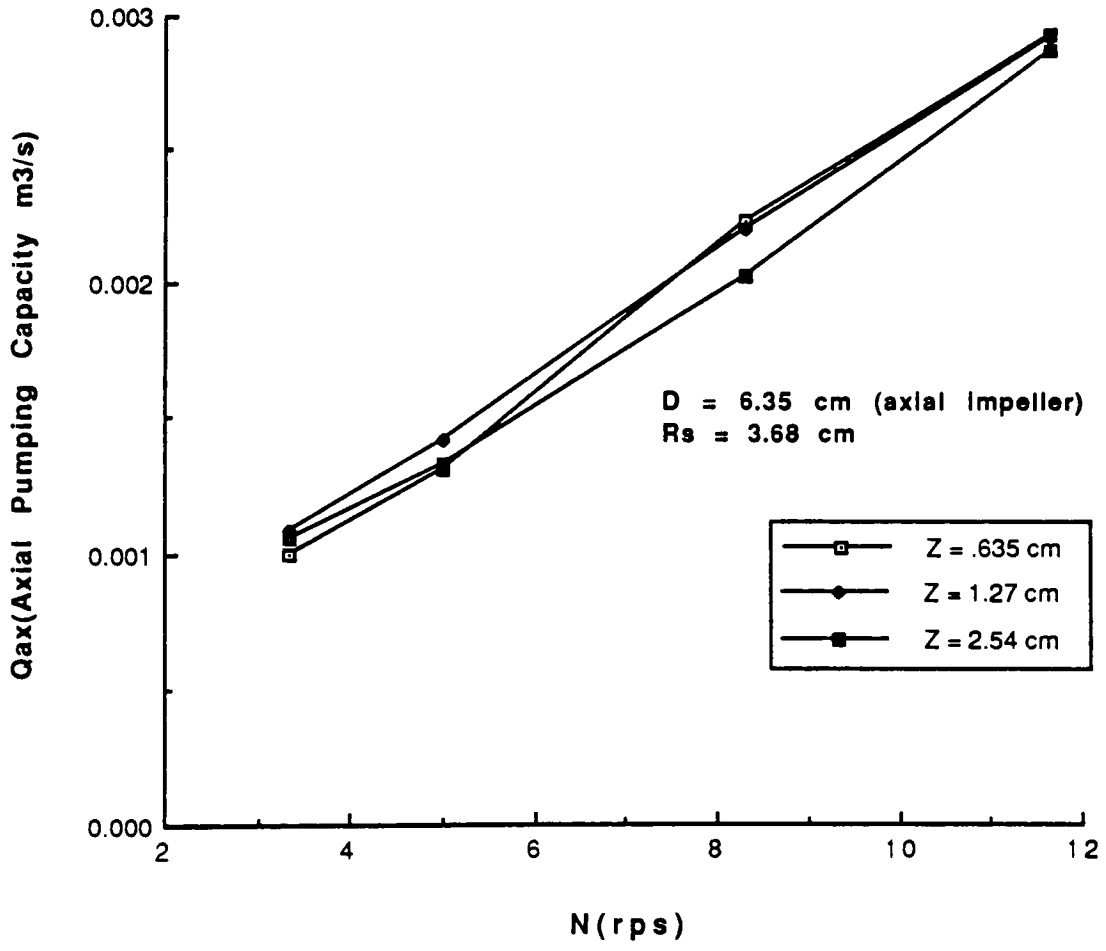


Figure 33: Axial Pumping Capacity vs. Impeller Speed  
Distance = Extended Range

Figures 32 and 33 both reveal that axial pumping rate is directly related to impeller speed, and relatively independent of z location over the range studied. The first finding is expected, as the speed of the impeller increases so does the fluid velocity and therefore the pumping rate. The second finding backs up the belief that axial impeller fluid flow emission doesn't have a great affect at generating fluid motion at appreciable distances above the impeller. Therefore, the impeller pumping rate remains constant or slightly decreases at distances above the impeller blade.

The axial pumping capacities on Figure 32 are seen to vary between  $.905ND^2$  and  $.971ND^2$ . Previous work as shown in Appendix E reveal that axial pumping capacities vary between  $.4ND^2$  and  $.96ND^2$ .

The apparent high pumping capacities in this research may be attributable to experimental error or to the fact that negative mean velocity values are seen as positive values by an LDA system which is operated without a frequency shifter. However, it must be noted that most of the previous works as given in Appendix E were done without state of the art equipment like LDA's. Therefore pumping capacity values of  $.905ND^2$  to  $.971ND^2$  may in actuality be more accurate than those reported by previous works.

A tabulation of historical pumping data is shown in Appendix E. Pumping capacities used in this table take the form of:

$$Q_{ax} = N_Q ND^2 \quad (48)$$

– where  $N_Q$  is called the Pumping Number and varies between 0.4 and 0.96.

In this experiment  $Q_{ax}$  taken over the length of the impeller blade at respective z locations of 0.635 cm, 1.27 cm, and 2.54 cm, yielded the following:

$$Q_{ax} = .952ND^2 \quad (49)$$

$$Q_{ax} = .971ND^2 \quad (50)$$

$$Q_{ax} = .905ND^2 \quad (51)$$

From these pumping capacities a mean  $Q_{ax}$  value of 0.943 can be realized with an average deviation of 3.6% and a maximum deviation of 4%.

Looking at  $Q_{ax}$  over the extended range,  $N_Q$  at  $z$  locations of 0.635 cm, 1.27 cm, and 2.54 cm, yields the following:

$$Q_{ax} = 1.084ND^2 \quad (52)$$

$$Q_{ax} = 1.127ND^2 \quad (53)$$

$$Q_{ax} = 1.081ND^2 \quad (54)$$

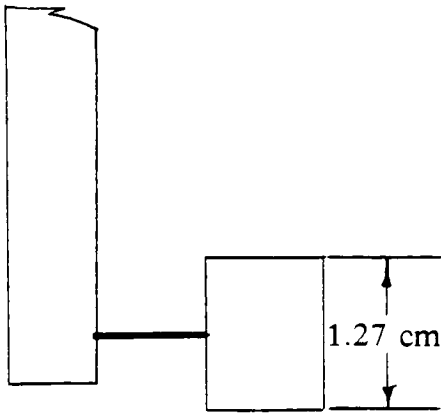
The above three  $Q_{ax}$  values have a mean of 1.097, an average deviation of 2.3% and a maximum deviation of 2.7%.

In comparing the  $N_Q$  values over the length of the impeller blade to the  $N_Q$  values over the extended range it becomes apparent that the majority of the pumping action occurs over the length of the blade. By comparing the mean  $N_Q$  value of 0.943 to the mean  $N_Q$  value of 1.097 it is seen that 85.6% of the axial flow generated by the axial impeller occurs over the length of the axial impeller.

#### **4.2.3 Radial Pumping Capacity**

Radial pumping capacities have traditionally been calculated over the height of the impeller blade. The following section provides pumping rate information calculated over the height of the impeller blade, and also over an extended range. The extended range was studied in order to look into momentum transfer and entrainment phenomena beyond the impeller zone. Figure 35 shows the two scenarios under study.

### BLADE LENGTH STUDY



### BROADER RANGE STUDY

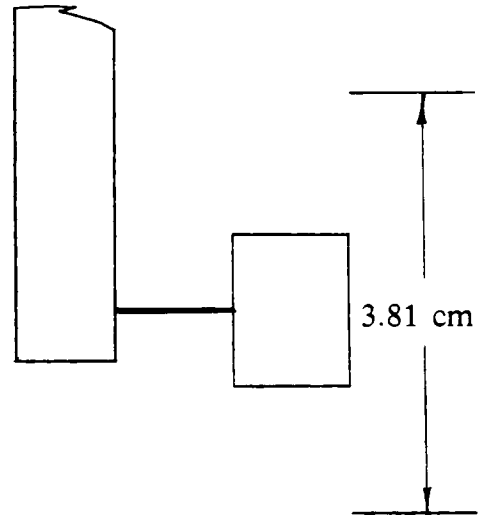


**Figure 34: Radial Pumping Capacity Area's of Study**

The actual radial pumping rates as a function of impeller speed are shown in Figures 35 and 36. The layout of these Figures is identical to those for the axial impeller case. The range in Figure 35 is from  $z = -.64$  cm to  $z = 0.64$  cm, while the range in Figure 36 is from  $-1.91$  cm to  $1.91$  cm. The radial impeller generates a sizeable fluid motion over the height of the impeller blade, and also entrains a rather sizeable amount of fluid over vertical distances above and below the blade. This is a major difference between the axial and the radial impeller under study.

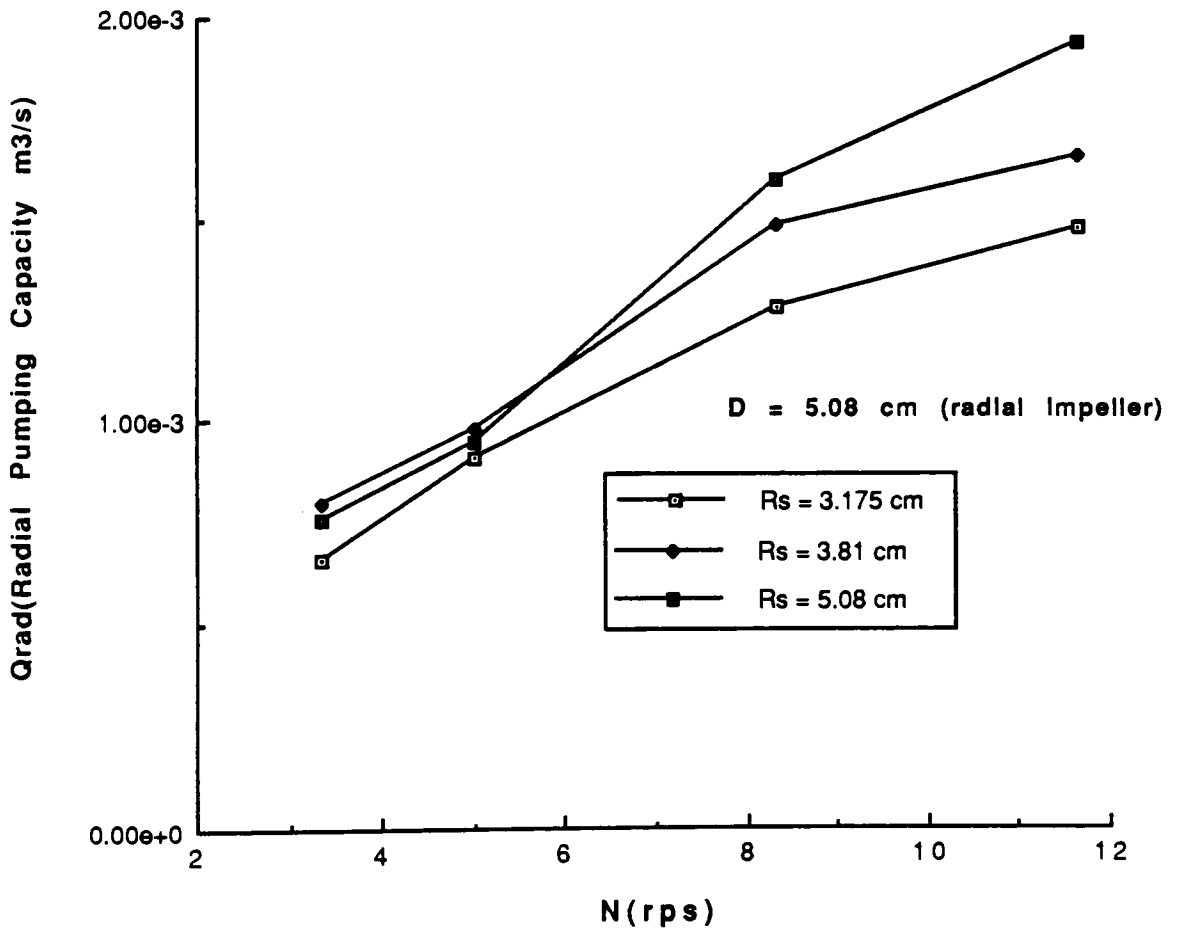


**Figure 35: Radial Pumping Capacity vs Impeller Speed  
Range = Height of Impeller Blade**

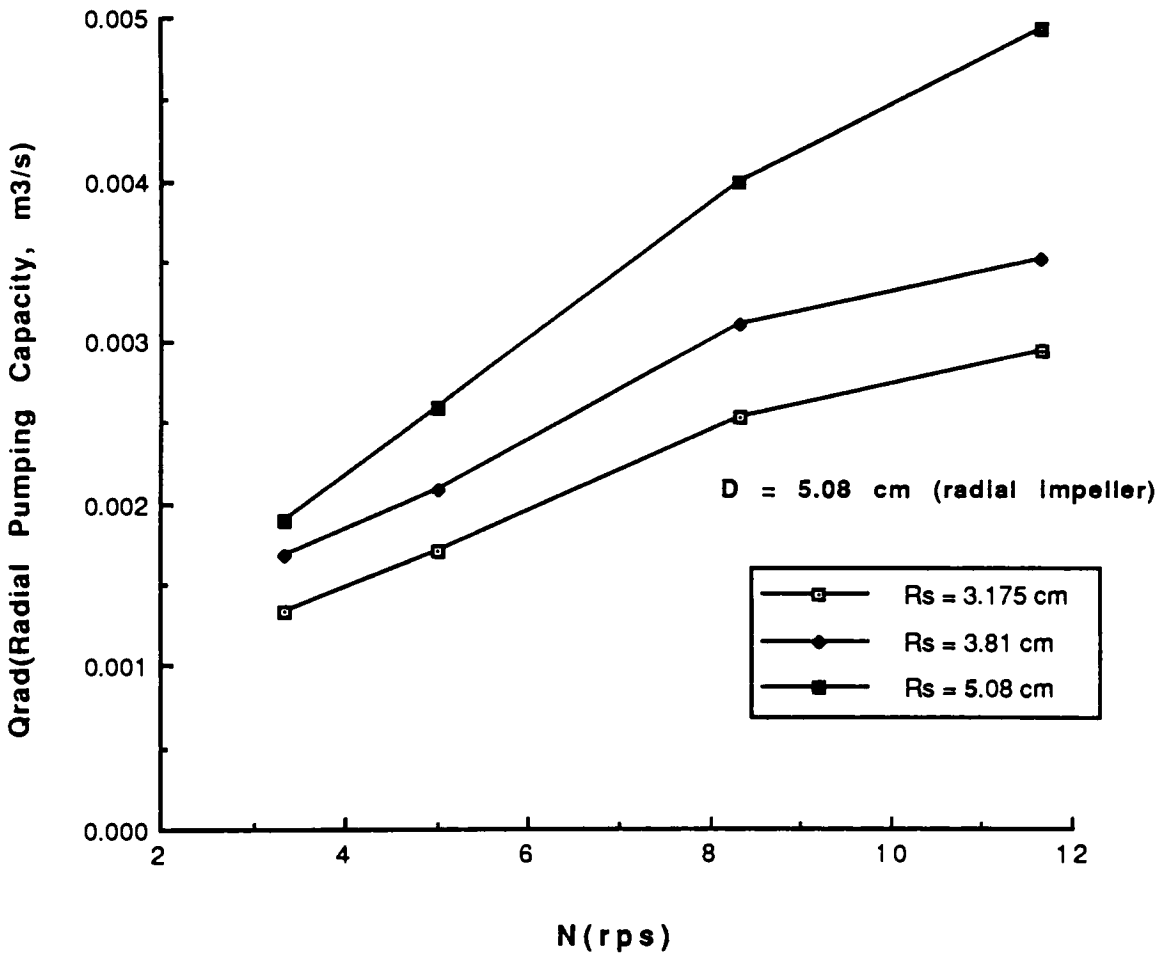


**Figure 36: Radial Pumping Capacity vs. Impeller Speed, Range = Extended Range**

Figures 35 and 36 both show that the radial pumping rate is directly related to impeller speed and that radial distance beyond the impeller blade has an appreciable effect upon the radial pumping rate. Cooper & Wolf (3) have shown similar variation of turbine pumping capacity in water as a function of impeller speed.

A tabulation of historical pumping data is shown in Appendix E. Pumping capacities used in this study take the form of:

$$Q_{\text{rad}} = N_Q ND^2 \quad (55)$$

– where  $N_Q$  varies between 0.54 and 1.4.

In this experiment  $Q_{\text{rad}}$  taken over the height of the impeller blade at respective “ $R_s$ ” locations of 3.175 cm, 3.81 cm, and 5.08 cm, yielded the following:

$$Q_{\text{rad}} = 0.95ND^2 \quad (56)$$

$$Q_{\text{rad}} = 1.08ND^2 \quad (57)$$

$$Q_{\text{rad}} = 1.10ND^2 \quad (58)$$

In looking at all three  $Q_{\text{rad}}$  values a mean  $Q_{\text{rad}}$  value of  $1.04ND^3$  results with an average deviation of 2.5% and a maximum deviation of 8.7%.

$Q_{\text{rad}}$  over the entire velocity profile, at “ $r_s$ ” locations of 3.175 cm, 3.81 cm, and 5.08 cm, is represented by the following:

$$Q_{\text{rad}} = 2.47ND^2 \quad (59)$$

$$Q_{\text{rad}} = 3.06ND^2 \quad (60)$$

$$Q_{\text{rad}} = 3.80ND^2 \quad (61)$$

The above three  $Q_{\text{rad}}$  values have a mean of 3.11, an average deviation of 21.4% and a maximum deviation of 22.2%.

By comparing  $N_Q$  values over the height of the impeller blade to  $N_Q$  values over the entire velocity profile it becomes apparent that radial flow impellers are capable of entraining large amounts of flow above and below the impeller blade. By comparing the mean  $N_Q$  value of 1.04 to the mean  $N_Q$  value of 3.11 it is apparent that only 33.4% of the radial flow generated by the radial flow impeller occurs over the height of the impeller.

### 4.3 Power Consumption

To measure the power consumed by an impeller, a torquemeter should ideally be utilized. As was stated in the theory section a torquemeter was originally employed, but for various reasons it was not useful for this experimental set-up.

Correspondingly, input power was calculated using the relationship  $P = IV$ , where  $I$  and  $V$  are measurable amperage and voltage quantities. It must be noted that two problems are apparent with this type of power calculation. First, when voltage or current spikes occur invalid results are measured, and secondly  $I$  and  $V$  values are so time dependent that accurate values are hard to discern from inaccurate values.

Figure 37 shows that over the range of impeller speeds, power consumption is seen to vary linearly with a slope of 1.1. Oldshue (14) and others, however, have shown that power vs. speed does indeed vary linearly, but with a slope of 3 and not 1.1. This is exemplified in Figures 38 and 39.

Referring to Figure 39 which shows  $N_p$  versus Reynolds Number it is seen that in the turbulent zone  $N_p$  values are relatively constant. The power numbers, as given above, lied within the turbulent zone, but were far from being constant.

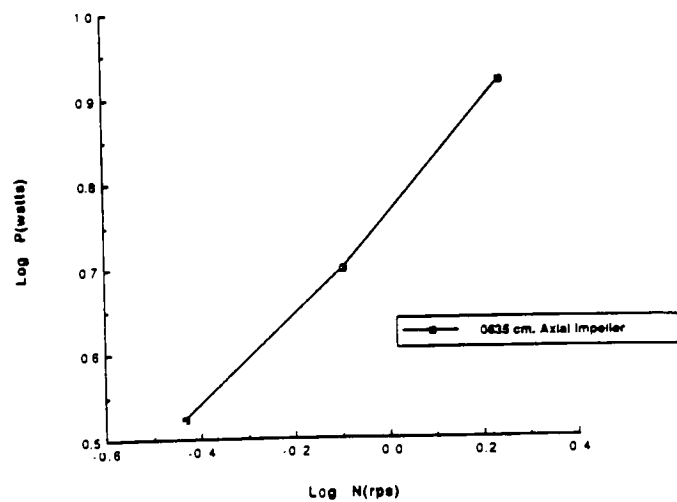


Figure 37: Power vs. Impeller Speed (Experimental)

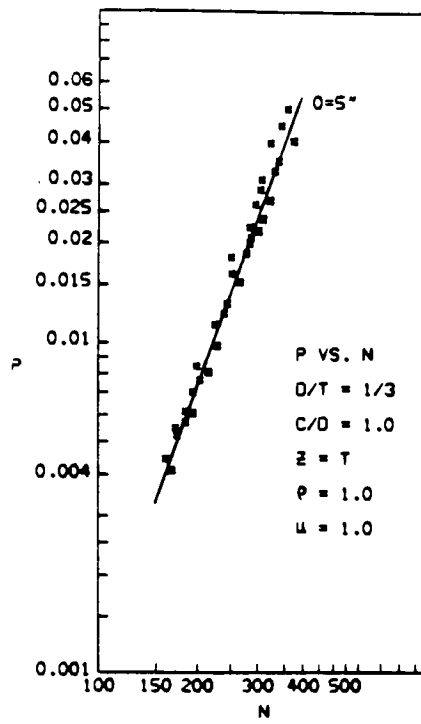


Figure 38: Power vs. Impeller Speed (Historical)

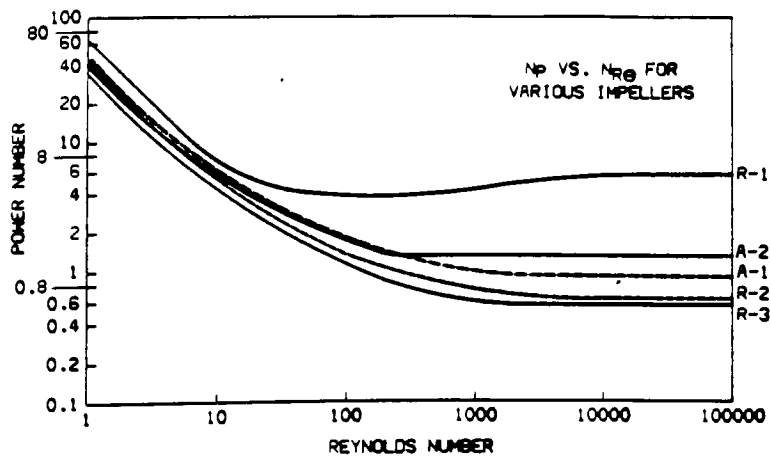


Figure 39:  $N_p$  vs.  $N_{Re}$  for Open Impellers

Correspondingly, when Oldshue's (14) experiment was again performed the same experiment is performed with differing impeller diameters, it was seen that power varies with impeller diameter to the fifth power. Figure 40 shows these results.

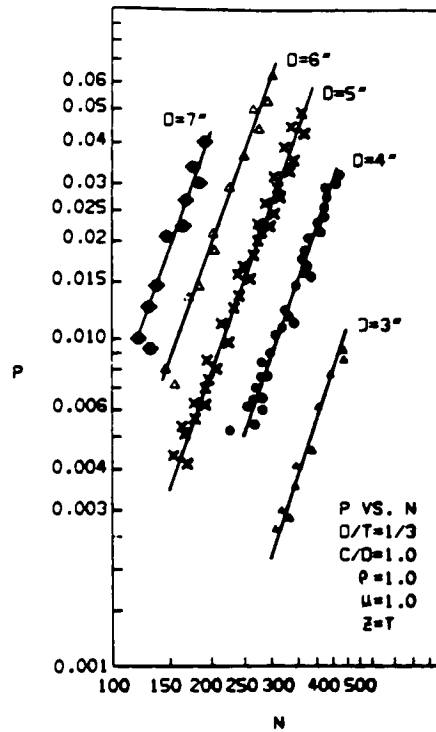


Figure 40:  $N_P$  vs.  $N_{Re}$  for Various Impeller Diameters

## 5.0 CONCLUSIONS

The intent of this thesis was to design, set-up, and use a mixing station for a fluid mixing study incorporating the use of an LDA. The majority of the findings put forth in this paper are corroborated by published data of previous workers. Listed below are the main conclusions of this study.

1. Axial and radial velocity profiles were found to be virtually identical to those of previous investigations.
2. Radial velocity profiles showed that as the measuring point was moved further from the tip of the impeller, the velocity profile became broader and flatter because of viscous fluid and momentum transfer effects.
3. Axial and radial pumping capacity values favorably compared to previously published values.
4. The majority of the flow generated by the axial impeller occurs closest to the impeller blades, in the so called "impeller zone".
5. At high impeller speeds the largest percentage of the axial and also the radial impeller tip velocity is transferred to the fluid flow.
6. 86% of the total flow generated by an axial impeller was shown to occur over the length of the axial impeller blade. While only 33% of the total flow generated by a radial impeller was shown to occur over the height of the impeller blade. This finding reveals that the radial impeller is very efficient at generating fluid motion at distances from the impeller itself.

## 6.0 APPENDIX

### 6.1 Appendix A — Mixing Impellers

The impellers as shown by Oldshue (1) are those most often employed in mixing tank experiments. The impellers labelled as R-1, A-1, and A-3 are the most popular of the impellers listed.

R1: This turbine type impeller is also referred as the Rushton turbine. It is used in applications where high shear or turbulence is required.

A1: This impeller is used primarily with smaller set-ups (.2 kw to 2.25 kw). It generates top to bottom or bottom to top axial flows.

A3: This impeller was designed to perform like the A-1 impeller but to outperform it in the following areas.

- 1) The A-3 is lighter than the A-1.
- 2) The A-3 is less expensive than the A-1.
- 3) The surface finish of the A-3 is smoother than the cast A-1.

Description of seven basic impellers		
Number	Name	Description
R-1	Flat blade	Vertical blades bolted to support disk
R-2	Bar turbine	Six blades bolted/attached to top and bottom of support disk
R-3	Anchor	Two blades with or without cross arm
A-1	Propeller	Constant pitch, standard three blades
A-2	Axial flow four blades	Constant angle at 45°
A-3	Axial flow three blades	Variable blade angle, near constant pitch
A-4	Double spiral	Two helical flights, pitch = 1/2D

## 6.2 Appendix B – Fluid Mixing System Description

A class 3b He-Ne Spectra Physics laser was used throughout this experiment. The laser was powered by a laser exciter which provided breakdown current to establish the lasing process.

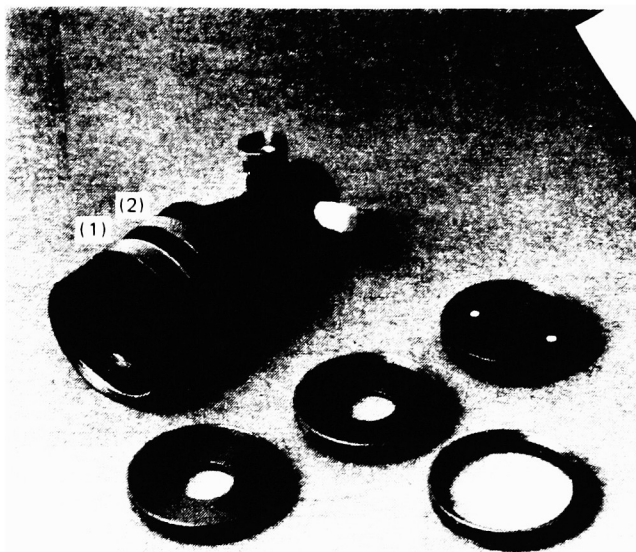
### Photomultiplier Section

A photomultiplier consists of four components; 1) the photo-cathode, 2) the input optics, 3) the dynode chain, and the 4) anode. The photo-cathode operates like a photovoltaic cell by “collecting” the scattered laser light electrons. The input optics then focus this scattered light onto the first dynode. The dynode chain acts like an amplifier to “multiply” the electron signal to a level equal to a constant raised to the number of dynodes. The anode collects the amplified electron signal and transports it to the counter module for processing.



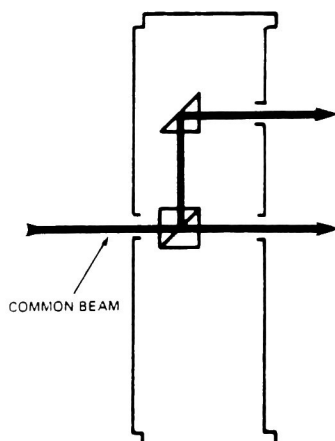
## Photo-Multiplier Optics

The Photo-Multiplier optics are used to focus the scattered laser light onto a pinhole, thru a filter to the photo-cathode of the photomultiplier. The scattered laser light is positioned onto the pinhole with the use of two locating screws positioned on the photomultiplier.



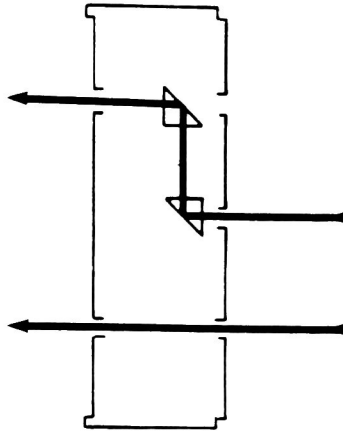
## Beamsplitter

The beamsplitter consists of a beamsplitter prism which splits the incoming laser source into two beams separated from one another by 30 mm.



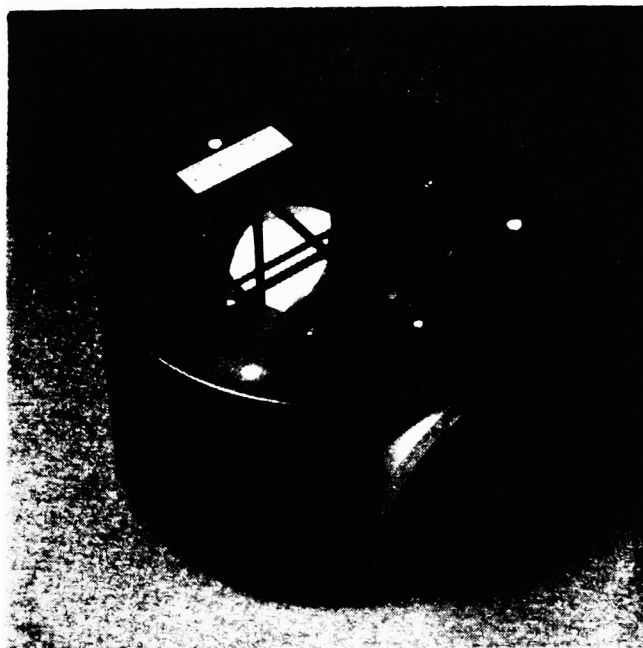
## Beam displacer

The beam displacer displaces one laser beam by an additional 30 mm, while leaving the second laser beam unaffected.



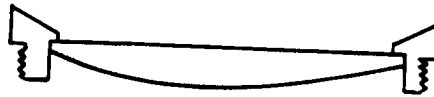
## Backscatter

The backscatter section is used in both one component differential mode and in two component modes. This section fixes the achromatic front lens and also collects the scattered laser signal and focuses it onto the photo-multiplier.



## Achromatic Front Lens

This lens has a 300 mm focal length, 79 mm aperture and is used strictly with backscatter LDA systems. The lens is coated with a hard anti-reflection coating with a reflectivity of less than .3% so that 99.7% of the scattered laser light can be focussed to the backscatter section.

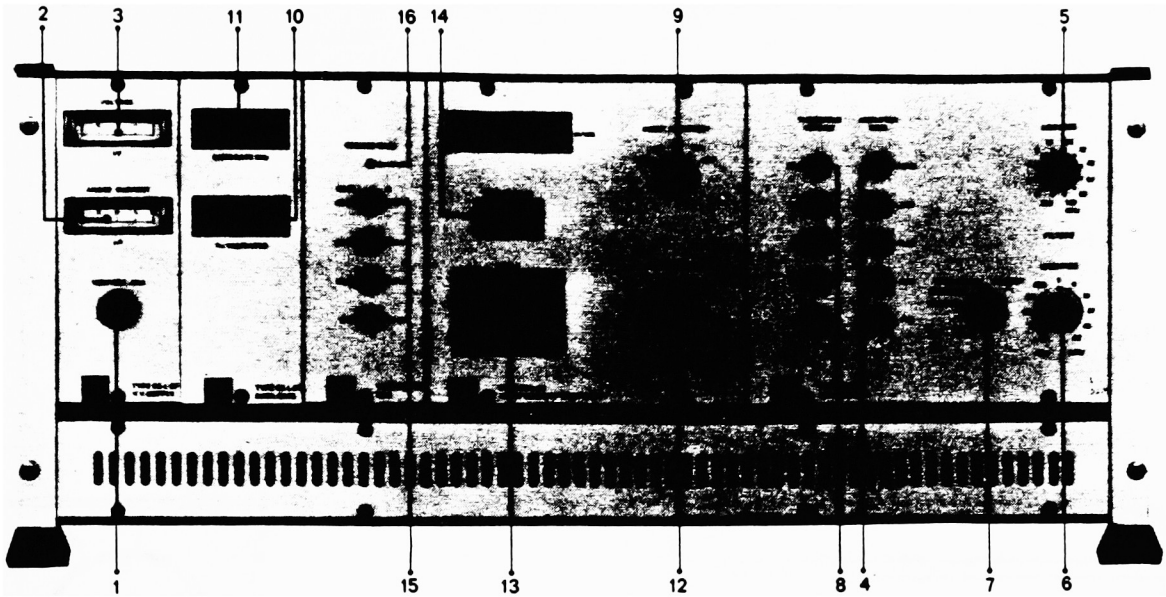


## LDA Counter Module

The frequency counter evaluates instantaneous velocity by measuring the time it takes a scattered particle to cross a number of interference fringes within a given measuring volume. The counter uses digital techniques by manipulating algorithms to calculate the mean velocity from the instantaneous velocity data. The following page shows the counter and it's various controls.

- 1) High Voltage Adjustment – for adjustment of photomultiplier voltage
- 2) Anode Current – reveals photomultiplier anode current in micro-amps
- 3) High Voltage Meter – reveals photomultiplier voltage in kV.
- 4) Amplifier Gain – regulates signal input gain levels

- 5) Low Pass Filter - removes high frequency noise
- 6) High Pass Filter - removes low frequency noise
- 7) Mode - sets the mode of operation
- 8) Threshold Window - sets upper amplitude threshold of the Doppler signal, which if exceeded will automatically reset the counter.
- 9) Comp. Accuracy - controls the data validation limits, i.e. the tolerance between the low count and the high count
- 10) Ensemble Width - determines the number of validated velocity calculations used in evaluating mean velocity values.
- 11) Scale Factor - sets the calibration factor for the Mean Velocity Computer
- 12) Velocity Display - digital display of the mean velocity values
- 13) Gain - analog output gain settings
- 14) Reduce Gain - lamp which signals when the analog output begins to overload.
- 15) 0/00 Validated - shows validated data in parts per thousand
- 16) Data Rate - displays sample rates in KHz.



## IBM PC

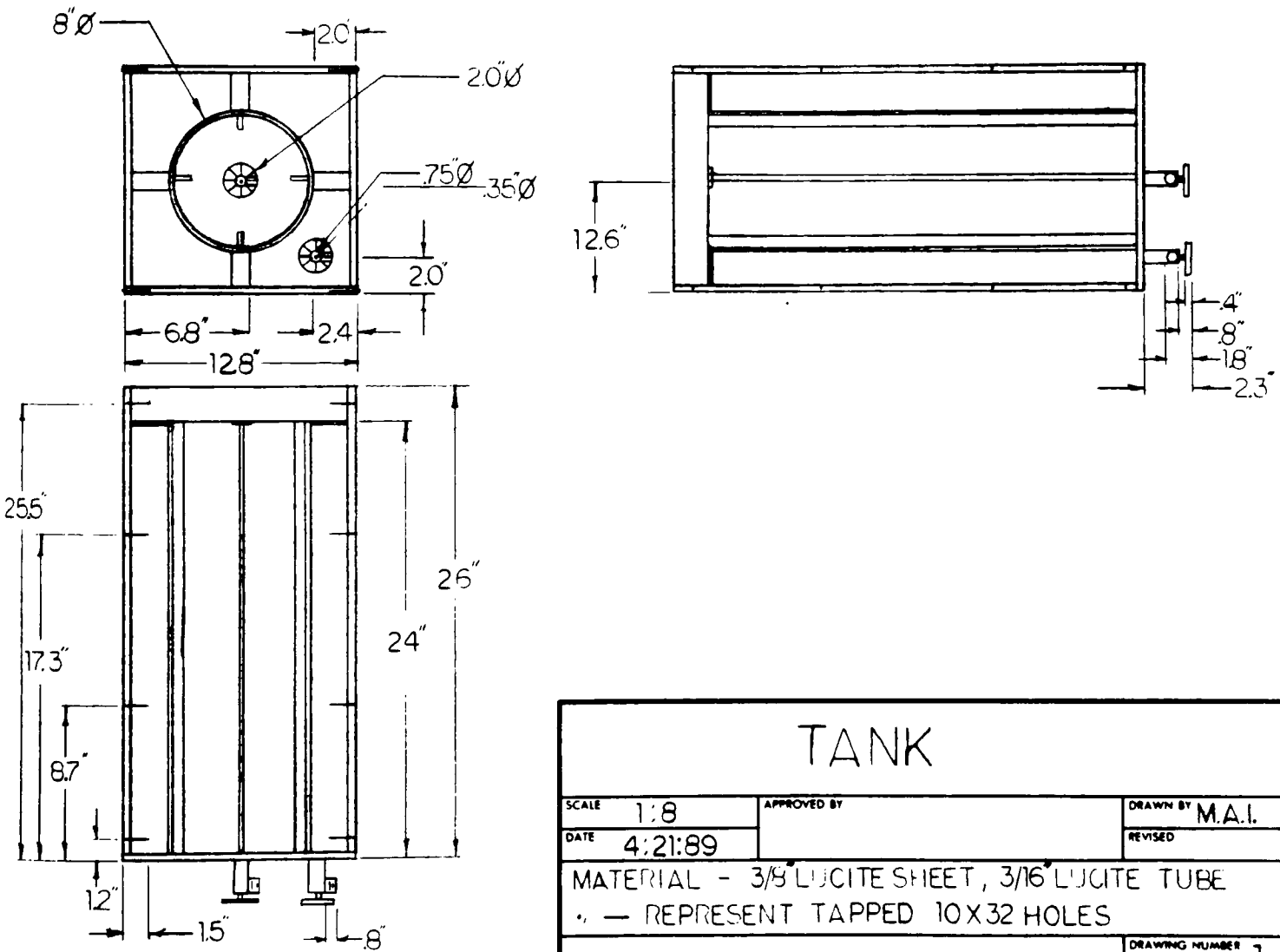
A HEI turbo XT IBM compatible personal computer with one 360k byte floppy drive and one 30 Mega-byte hard disk drive was used. The system also utilizes a Definition EGA monitor and an EPSON LX-800 printer for visual and hardcopy output.

Two-channel LDA software was employed on this system in order to generate mean velocity values, turbulence values, and mean velocity profiles.

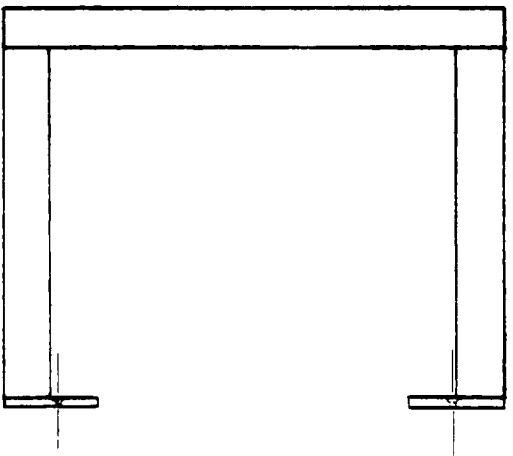
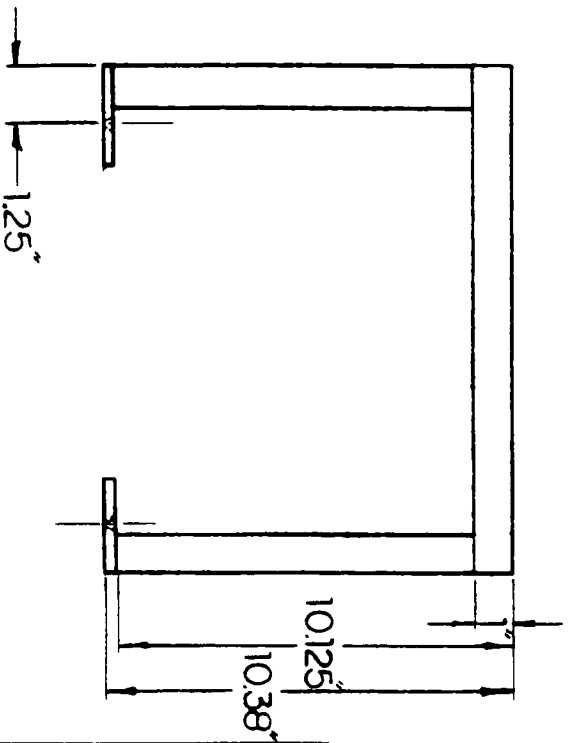
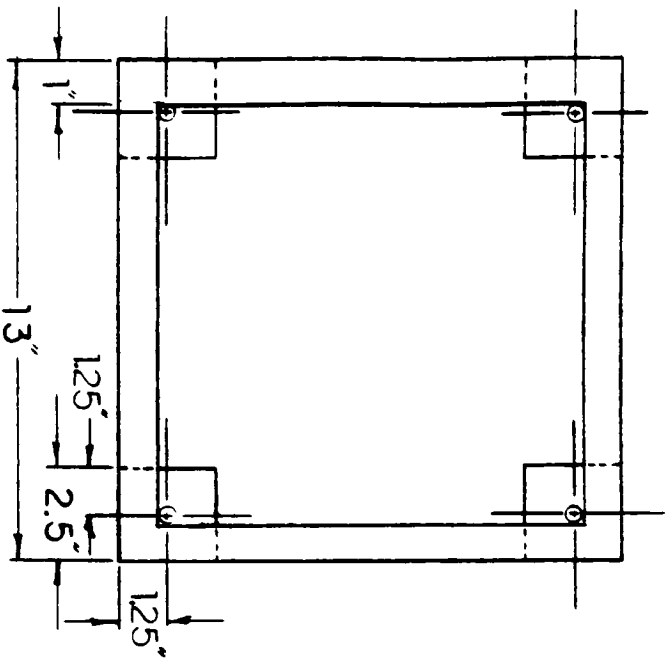
## Traverse

The LDA optics system, was manipulated through the use of a manually operated 3-D traversing system. The traverse had a Z range of 33", a Y range of 16", and an X range of 16".

6.3 Appendix C — Detailed Mixing Station Design Drawings

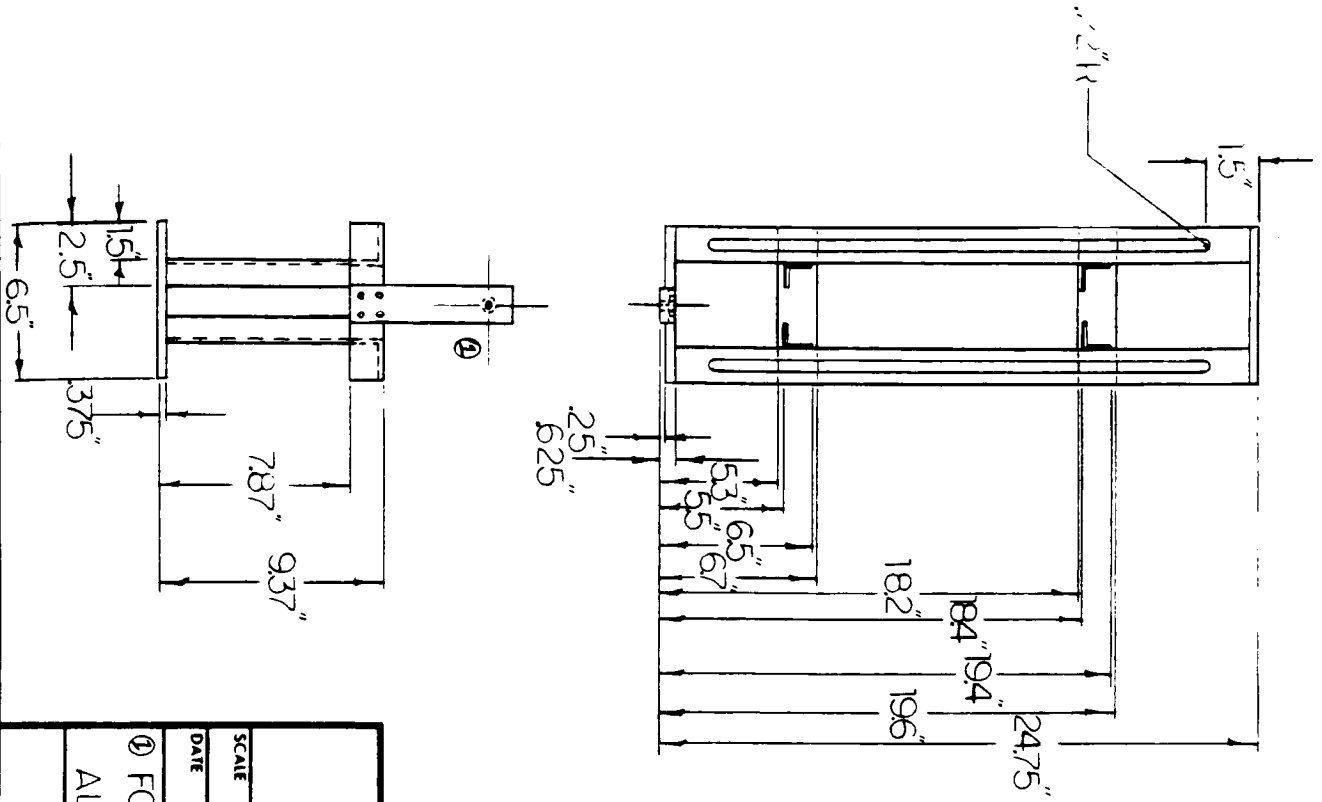


<h1>TANK</h1>		
SCALE 1:8	APPROVED BY	DRAWN BY M.A.I.
DATE 4:21:89		REVISED
MATERIAL - 3/8" LUCITE SHEET, 3/16" LUCITE TUBE • — REPRESENT TAPPED 10X32 HOLES		
		DRAWING NUMBER 7



# TANK STAND

SCALE		APPROVED BY	
1:5			
DATE		DRAWN BY	
4:7:89		M.A.I.	
MATERIAL - 1/8" THICK ANGLE IRON, 25" THICK STEEL SHEET			
DRAWING NUMBER		REVISED	
2			

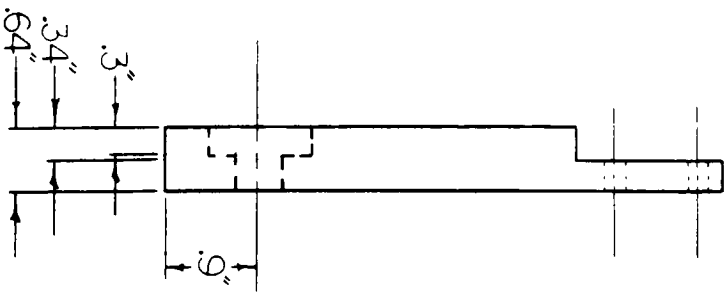
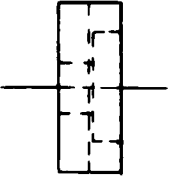
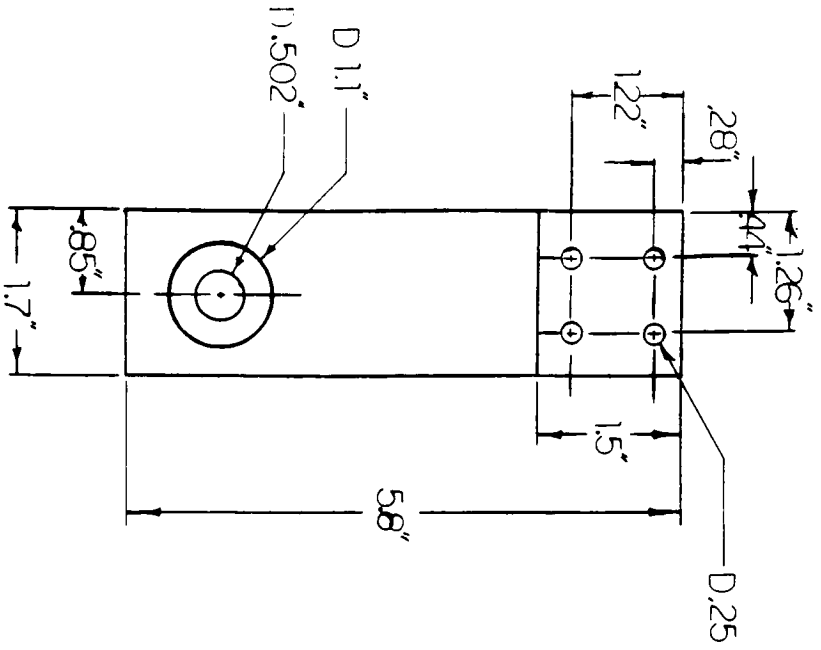


# WALL CANTILEVER

SCALE	1:8	APPROVED BY	
DATE	4-25-89	DRAWN BY	MAL
		REVISED	

① FOR DIMENSIONS SEE DRAWING 4  
 ALL ANGLE IRON 1/8" THICK

DRAWING NUMBER  
3



# CANTILEVER BEARING

SCALE 1:2

APPROVED BY

DATE

4-25-89

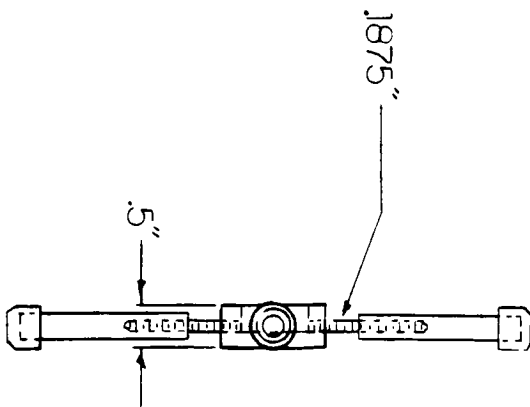
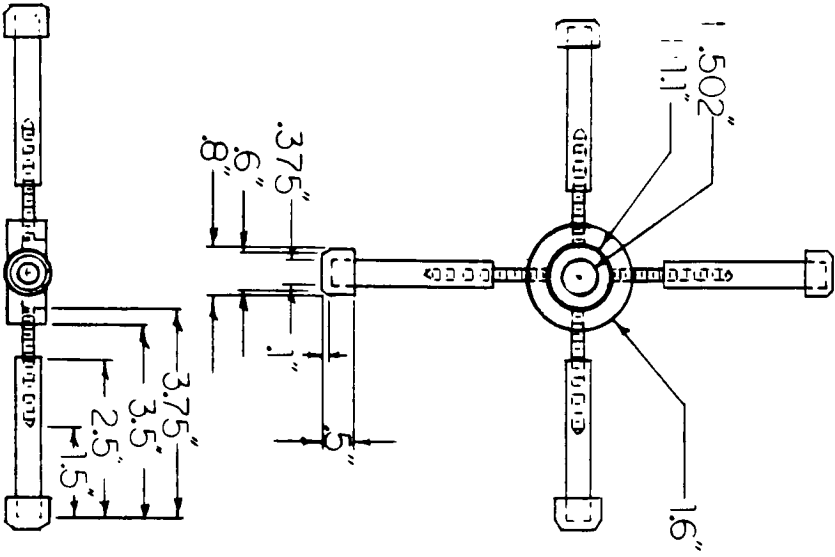
DRAWN BY M.A.L

REVISED

MATERIAL - ALUMINUM

DRAWING NUMBER

4



# TUBE BEARING

SCALE 1:3

DATE 4:5:89

APPROVED BY

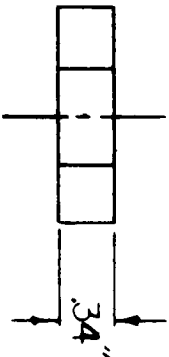
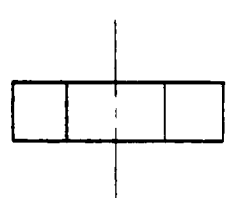
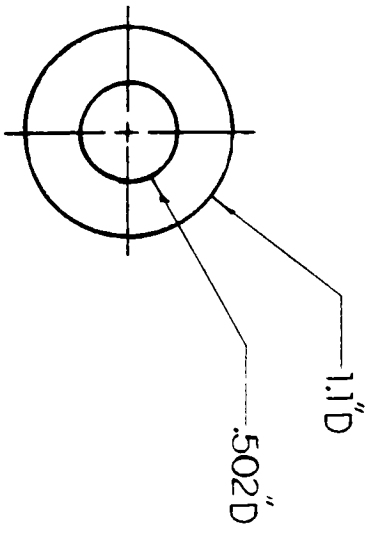
DRAWN BY MAJ.

REVISED

MATERIAL - 10X30 HILFALTI 9 TELL KOD,  
BIAA PCK, 1 M

DRAWING NUMBER

5

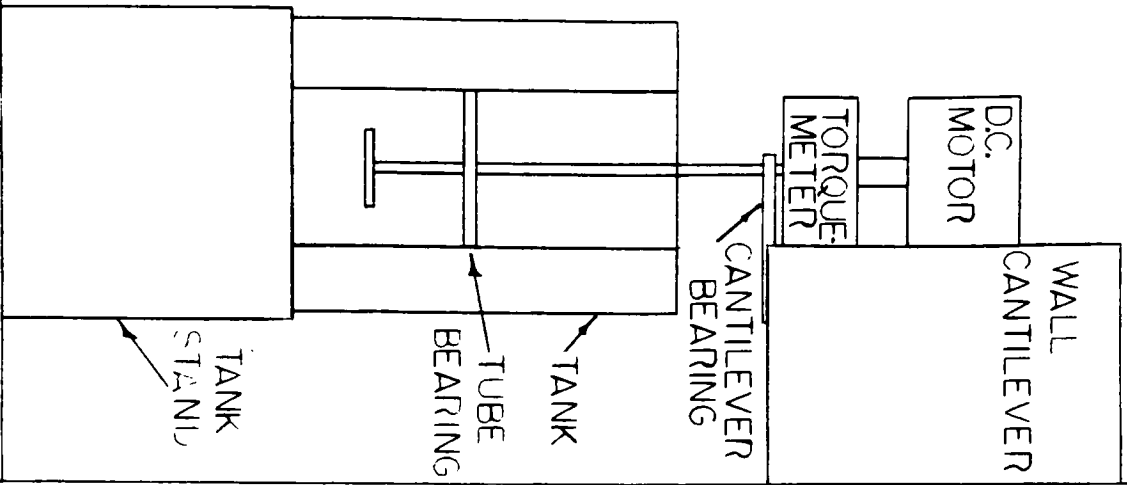


# BEARING

SCALE	1:1	APPROVED BY	DRAWN BY
DATE	4-30-89		MAL

USED IN: THE TUBE BEARING (drawing 3)  
THE CANTILEVER BEARING (drawing 4)

DRAWING NUMBER  
6



SUPPORTING  
WALL

ASSEMBLY DRAWING

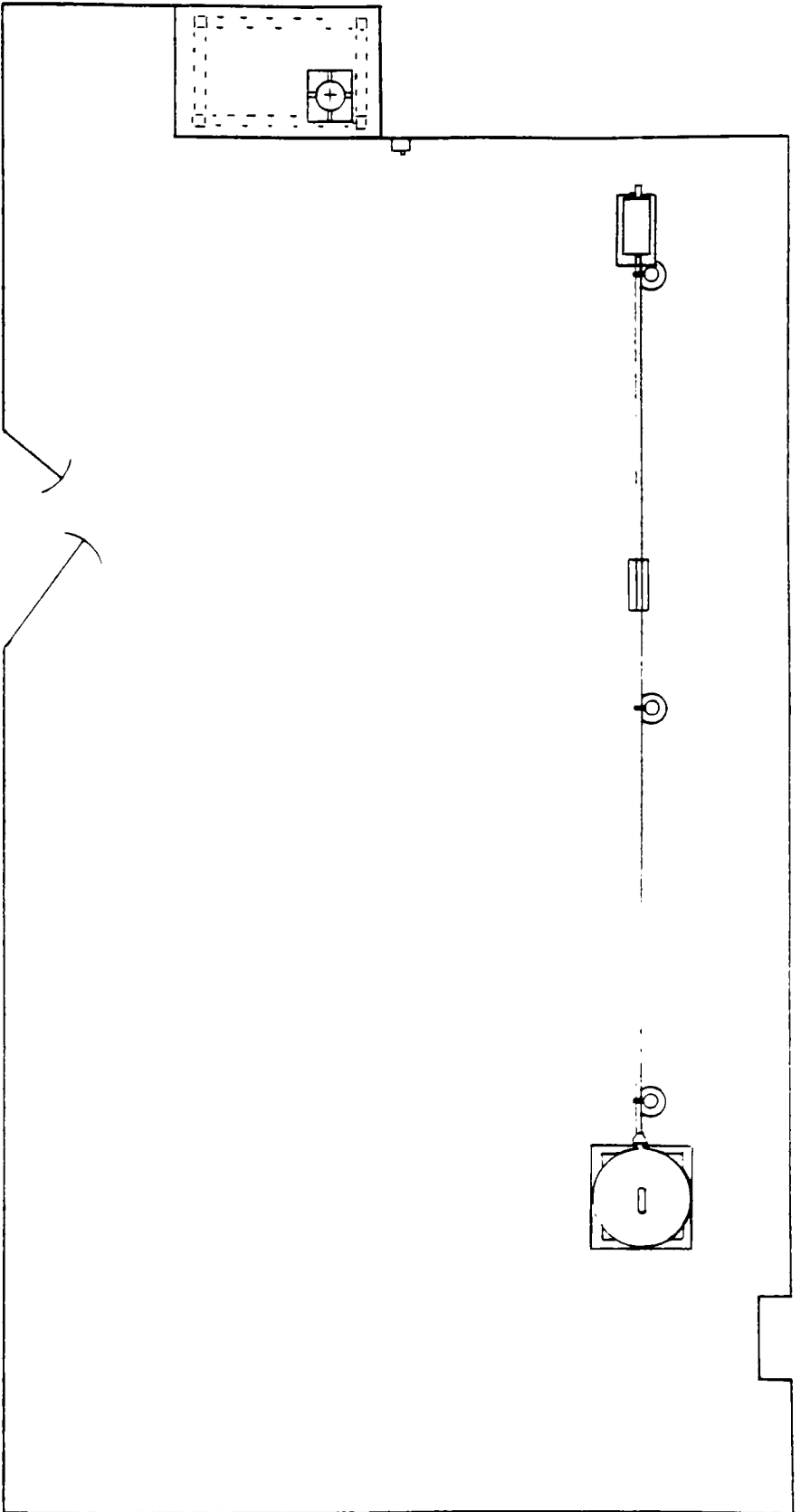
SCALE \_\_\_\_\_  
DATE 5:7:89

APPROVED BY \_\_\_\_\_

DRAWN BY MAI  
REVISED \_\_\_\_\_

DRAWING NUMBER

7



# FLOOR PLAN

SCALE 1" = 4'

APPROVED BY

DRAWN BY MAL

DATE 5.7.89

REVISED

PLAN SHOWS MIXING TANK AND FLOW EXPERIMENT

DRAWING NUMBER

8



## 6.4 Appendix D — Experimental Runs

### AXIAL VELOCITY PROFILES GENERATED BY AN AXIAL IMPELLER

RUN	RPM	PROBE VOLUME POSITION
Jun52Qax	200	0.25" above the impeller tip-
Jun52Hax	200	0.50" above the impeller tip-
Jun52Oax	200	1.00" above the impeller tip
Jun53Qax	300	0.25" above the impeller tip-
Jun53Hax	300	0.50" above the impeller tip-
Jun53Oax	300	1.00" above the impeller tip
Jun55Qax	500	0.25" above the impeller tip-
Jun55Hax	500	0.50" above the impeller tip-
Jun55Oax	500	1.00" above the impeller tip
Jun57Qax	700	0.25" above the impeller tip-
Jun57Hax	700	0.50" above the impeller tip-
Jun57Oax	700	1.00" above the impeller tip

### RADIAL VELOCITY PROFILES GENERATED BY AN AXIAL IMPELLER

RUN	RPM	PROBE VOLUME POSITION
Jun52Qrad	200	0.25" beyond the impeller tip-
Jun52Hrad	200	0.50" beyond the impeller tip-
Jun52Orad	200	1.00" beyond the impeller tip
Jun53Qrad	300	0.25" beyond the impeller tip-
Jun53Hrad	300	0.50" beyond the impeller tip-
Jun53Orad	300	1.00" beyond the impeller tip
Jun55Qrad	500	0.25" beyond the impeller tip-
Jun55Hrad	500	0.50" beyond the impeller tip-
Jun55Orad	500	1.00" beyond the impeller tip
Jun57Qrad	700	0.25" beyond the impeller tip-
Jun57Hrad	700	0.50" beyond the impeller tip-
Jun57Orad	700	1.00" beyond the impeller tip

## AXIAL VELOCITY PROFILES GENERATED BY AN AXIAL IMPELLER

RUN	RPM	PROBE VOLUME POSITION
Jun72Qax	200	0.25" above the impeller tip-
Jun72Hax	200	0.50" above the impeller tip-
Jun72Oax	200	1.00" above the impeller tip
Jun73Qax	300	0.25" above the impeller tip-
Jun73Hax	300	0.50" above the impeller tip-
Jun73Oax	300	1.00" above the impeller tip
Jun75Qax	500	0.25" above the impeller tip-
Jun75Hax	500	0.50" above the impeller tip-
Jun75Oax	500	1.00" above the impeller tip
Jun77Qax	700	0.25" above the impeller tip-
Jun77Hax	700	0.50" above the impeller tip-
Jun77Oax	700	1.00" above the impeller tip

## RADIAL VELOCITY PROFILES GENERATED BY A RADIAL IMPELLER

RUN	RPM	PROBE VOLUME POSITION
Jun52Qrad	200	0.25" beyond the impeller tip-
Jun52Hrad	200	0.50" beyond the impeller tip-
Jun52Orad	200	1.00" beyond the impeller tip
Jun53Qrad	300	0.25" beyond the impeller tip-
Jun53Hrad	300	0.50" beyond the impeller tip-
Jun53Orad	300	1.00" beyond the impeller tip
Jun55Qrad	500	0.25" beyond the impeller tip-
Jun55Hrad	500	0.50" beyond the impeller tip-
Jun55Orad	500	1.00" beyond the impeller tip
Jun57Qrad	700	0.25" beyond the impeller tip-
Jun57Hrad	700	0.50" beyond the impeller tip-
Jun57Orad	700	1.00" beyond the impeller tip

In general, any given run can be evaluated by its alphanumeric description. The first three letters and alphanumeric character represent the month and day the run was completed. The final numerical character stands for the impeller speed in hundreds of rpm's. The sixth alpha character represents the distance the probe volume was above or beyond the impeller tip (Q = .25", H = .50", and O = 1.0"); while the final three alpha characters stand for what kind of profile was taken.

The forty eight runs were completed in order to gain insight into the following conditions.

- 1) The effect speed has on velocity profile and pumping capacity.
- 2) The velocity profile shape and pumping capacity value at various distances above or beyond the impeller tip.
- 3) The type of radial velocity profile which could be generated by a radial impeller as well as an axial impeller.
- 4) The type of axial velocity profile which could be generated by a radial impeller as well as an axial impeller.

## 6.5 Appendix E — Historical Axial and Radial Pumping Data

Experimentally determined flow numbers for axial-flow impellers

	Z/T	C/T	Number of baffles	B/T	D/T	W/D	$\beta$ or pitch ratio	Number of blades	$N_p$	$N_Q$
<b>MARINE PROPS</b>										
Missenard-Quint		1	3	.1	.33		1.0	3	.37	0.55
Ekato		↓	3	↓	↓		↓	↓	.35	—
Moritz		↓	4	↓	↓		↓	↓	.35	0.50
LIGHTNIN		↓	4	↓	↓		↓	↓	.32	—
Uhl and Gray (29)		↓	4	↓	↓		—	↓	—	0.50
Nagata (14)		—	8	↓	.50		—	↓	60	0.43
Cooper and Wolf (4)		—	4	↓	.53		—	↓	—	0.53
Rushton and Oldshue (25)		—	—	—	—		1.0	↓	—	0.40
Marr (13)	.7-1.1	.4-.8	3	—	.2-.6		—	↓	—	0.61
Fort et al. (11)	1.0	—	—	—	.2-.33		—	↓	—	0.52
Consensus									.33-.37	.40-55
<b>Pitch-blade turbine</b>										
Bruxelmane	—	1	4	.1	.33	.20	45°	4	1.5	0.75
<b>LIGHTNIN</b>										
Missenard-Quint	—	1	4	↓	↓	.20	↓	4	1.27	0.79
Ekato	—	1	2	↓	↓	.28	↓	6	4.1	0.87
Fort et al. (11)	—	.17-.34	3	↓	↓	.25	↓	↓	2.0	—
Uhl and Gray (29)	—	1	4	↓	↓	.20	↓	↓	1.6	0.96
Nagata (14)	—	1	4	↓	↓	.176	↓	↓	1.3	—
Nagata (14)	1.0	—	8	—	.50	.10	↓	8	0.72	0.31
Nagata (14)	1.0	—	8	.1	.50	.10	↓	8	2.8	0.87
Fort et al. (11)	1.0	—	4	.1	.20-.33	.20	24°	3	—	0.48
Shaped blades	—	0.5	3	.1	.667	DNA	—	3	.43	.64
Orange MIG		3 impeller	4	.1	.7	—	—	2	.6	—
		↓	4	.1	.8	—	—		.4	—
		↓	0	—	.9	—	—		.2	—
Intermig		↓	3	.1	.7	—	—		.8	—
Missenard-Quint	MIG type	.5	3	.1	.667			2	.32	.58
	MIG type		4	.1	.71			2	.30	—
Mixer—TT			3	.1	.25-.50	DNA		3	—	.96
TTM			↓	↓	↓	—		↓	—	.37
EXP			↓	↓	↓	—		↓	—	.47

### Experimentally determined flow numbers for axial-flow impellers

	Z/T	C/T	Number of baffles	B/T	D/T	W/D	$\beta$ or pitch ratio	Number of blades	$N_p$	$N_Q$
<b>MARINE PROPS</b>										
Missenard-Quint		1	3	.1	.33		1.0	3	.37	0.55
Ekato		↓	3	↓	↓		↓	↓	.35	—
Moritz			4	↓	↓		↓	↓	.35	0.50
LIGHTNIN			4	↓	↓		↓	↓	.32	—
Uhl and Gray (29)			4	↓	↓		—	↓	—	0.50
Nagata (14)		—	8	↓	.50		—	↓	.60	0.43
Cooper and Wolf (4)			4		.53		—	↓	—	0.53
Rushton and Oldshue (25)			—		—		1.0	↓	—	0.40
Marr (13)	.7-1.1	.4-.8	3		.2-.6		—	↓	—	0.61
Fort et al. (11)	1.0				.2-.33		—	↓	—	0.52
Concensus									.33-.37	.40-.55
<b>Pitch-blade turbine</b>										
Bruxelmane	—	1	4	.1	.33	.20	45°	4	1.5	0.75
<b>LIGHTNIN</b>										
Missenard-Quint	—	1	4	↓	↓	.20	↓	4	1.27	0.79
Ekato	—	.17-.34	2	↓	↓	.28	↓	6	4.1	0.87
Fort et al. (11)	—	1	3	↓	↓	.25	↓	↓	2.0	—
Uhl and Gray (29)	—	1	4	↓	↓	.20	↓	↓	1.6	0.96
Nagata (14)	1.0	—	4	↓	↓	.176	↓	↓	1.3	—
Nagata (14)	1.0	—	0	—	.50	.10	↓	8	0.72	0.31
Nagata (14)	1.0	—	8	.1	.50	.10	↓	8	2.8	0.87
Fort et al. (11)	1.0	—	4	.1	.20-.33	.20	24°	3	—	0.48
Shaped blades	—	0.5	3	.1	.667	DNA	—	3	.43	.64
<b>Orange MIG</b>										
		3 impeller	4	.1	.7	—	—	2	.6	—
		↓	4	.1	.8	—	—		.4	—
			0	—	.9	—	—		.2	—
Intermig		↓	3	.1	.7	—	—		.8	—
<b>Missenard-Quint</b>										
	MIG type	.5	3	.1	.667			2	.32	.58
	MIG type		4	.1	.71			2	.30	—
<b>Mixer—TT</b>										
	TTM		3	.1	.25-.50	DNA		3	—	.96
	EXP		↓	↓	↓	—		↓	—	.37
						—			—	.47

## 6.6 Appendix F — FORTRAN Program for Calculating Pumping Capacity Values

```
0001 C *****
0002 C * RADIAL PUMPING RATE INTEGRATION *
0003 C * using Simpson's 1/3 rule *
0004 C *****
0005 program radial pumping
0006 INTEGER N,MAXN
0007 PARAMETER (MAXN = 100)
0008 REAL*4 A,B,H,QRA,V(MAXN),XE,XO,RS
0009 WRITE(6,*)'INPUT THE NUMBER OF VELOCITY DATA POINTS'
0010 READ(5,*)N
0011 WRITE(6,*)'INPUT THE LEFTMOST VELOCITY VALUE IN M/S'
0012 READ(5,*)A
0013 WRITE(6,*)'INPUT THE RIGHTMOST VELOCITY VALUE IN M/S'
0014 READ(5,*)B
0015 WRITE(6,*)'INPUT THE RS VALUE IN METERS'
0016 READ(5,*)RS
0017 WRITE(6,*)'INPUT THE STEP SIZE IN METERS'
0018 READ(5,*)H
0019 DO I=2,N-1,1
0020     WRITE(6,*)'INPUT THE NEXT VELOCITY VALUE, FROM LEFT TO RIGHT'
0021     READ(5,*)V(I)
0022 ENDDO
0023 XE = 0.
0024 XO = 0.
0025 DO I=2,N,2
0026     XE = XE + V(I)
0027 ENDDO
0028 DO I=3,N-1,2
0029     XO = XO + V(I)
0030 ENDDO
0031 QRA = (H/3)*(A + B + 4*XE + 2*XO)*2*RS*3.141592654
0032 WRITE(6,*)'THE RADIAL PUMPING RATE, IN M/SEC, IS: ',QRA
0033 STOP
0034 END
```

```

0001 C *****
      C * AXIAL PUMPING RATE INTEGRATION *
0003 C * - using Simpson's 1/3 rule *
0004 C *****
0005 program axial pumping
0006 INTEGER N,MAXN
0007 PARAMETER (MAXN = 100)
0008 REAL*4 A,B,H,QAX,V(MAXN),XE,XO,RS,RSS
0009 WRITE(6,*)'INPUT THE NUMBER OF VELOCITY DATA POINTS'
0010 READ(5,*)N
0011 WRITE(6,*)'INPUT THE LEFTMOST VELOCITY VALUE IN M/S'
0012 READ(5,*)A
0013 WRITE(6,*)'INPUT THE RIGHTMOST VELOCITY VALUE IN M/S'
0014 READ(5,*)B
0015 WRITE(6,*)'INPUT THE FIRST RS VALUE IN METERS'
0016 READ(5,*)RS
0017 WRITE(6,*)'INPUT THE STEP SIZE IN METERS'
0018 READ(5,*)H
0019 DO I=2,N-1,1
0020     WRITE(6,*)'INPUT THE NEXT VELOCITY VALUE, FROM LEFT TO RIGHT'
0021     READ(5,*)V(I)
0022 ENDDO
0023 XE = 0.
0024 XO = 0.
0025 RSS = RS + H
0026 DO I=2,N-1,2
0027     XE = XE + 4*RSS*V(I)
0028     RSS = RSS + 2*H
0029     WRITE(6,*)XE
0030 ENDDO
0031 RSS = RS
0032 DO I=3,N-2,2
0033     RSS = RSS + 2*H
0034     XO = XO + 2*RSS*V(I)
0035     WRITE(6,*)XO
0036 ENDDO
0037 RSS = RSS + 2*H
0038 QAX = (H/3)*(RS*A + RSS*B + XE + XO)*4*3.141592654
0039 WRITE(6,*)'THE AXIAL PUMPING RATE, IN M/SEC, IS: ',QAX
0040 STOP
0041 END

```

## 7.0 BIBLIOGRAPHY

- 1) Bertrand, J., Couderc, J.P., Angelino, H., "Power Consumption, Pumping Capacity and Turbulence Intensity in Baffled Stirred Tanks: Comparison Between Several Turbines," Chemical Engineering Science, Vol. 35, 157 - 159, January 1980.
- 2) Bowen, R.L., "Unraveling the Mysteries of Shear Sensitive Mixing Systems," Chemical Engineering, 55, 57-59, 61,63, June 9, 1986.
- 3) Cooper, R.G., Wolf, D., "Velocity Profiles and Pumping Capacities for Turbine Type Impellers," Canadian Journal of Chemical Engineering, Vol. 46, 94-100, April 1968.
- 4) Cutter, L.A., "Flow and Turbulence in a Stirred Tank," A.I.Ch.E. Journal, Vol. 12, No. 1, 35,38,40,43, January 1966.
- 5) Dickey, D.S. and Fenic, J.G., "Dimensional Analysis for Fluid Agitation Systems," Chemical Engineering, 139 - 142, January 5, 1976.
- 6) Gray, D.J., Treybal, R.E., Barnett, S.M., "Mixing of Single and Two Phase Systems: Power Consumption of Impellers," A.I.Ch.E. Journal, Vol 28, No 2, 196-198, March 1982.
- 7) Gunkel, A.A., Weber, M.E., "Flow Phenomena in Stirred Tanks," A.I.Ch.E. Journal, Vol. 21, No. 5, 931-932, September, 1975.
- 8) Holmes, D.B., Voncken, R.M., Dekker, J.A., "Fluid Flow in Turbine Stirred, Baffled Tanks," Chemical Engineering Science, Vol. 19, 201-202, 206-207, 1964
- 9) Mahouast, M, Cagnet, G. "Analysis of Turbulent Mixing in a CFSTR From LDV Measurements," Institute National Polytechnique de Lorraine.
- 10) Marr, G.R., Johnson, E.F., "The Pumping Capacity of Impellers in Stirred Tanks," A.I.Ch.E. Journal, Vol. 9, No. 38, 383-385, May 1963.
- 11) Menon, Rajan, "Laser Doppler Velocimetry: Performance and Applications," American Laboratory, 2-3, February 1982.
- 12) Oldshue, J.Y., "Mixing Processes in the Protective Coating Industry," Journal of Paint Technology, Volume 40, No. 517, 68, 74-77, February 1968.
- 13) Oldshue, J.Y., Fluid Mixing Technology, McGraw Hill, NY, NY, Chap 1,3,8, 1983.
- 14) Oldshue, J.Y., "Scale-up of Unique Industrial Mixing Processes," 5th European Conference on Mixing, Paper 7, 37-38, 45-56, 48, June 1985. Conference on Mixing, Paper 7, 37-38, 45-56, 48, June 1985.
- 15) Oldshue, J.Y., and Herbst, N.R. "A Guide to Fluid Mixing" 1-11, 1990.
- 16) Oldshue, J.Y., and Rushton, J.H., "Mixing Present Theory and Practice," Chemical Engineering Progress, Volume 49, Number 4, 161, 1953.
- 17) Rushton, J.H, D.E. Mack, and H.J. Everett, Trans. Am. Inst. Chem. Engrs., 42, 441 (1946).

- 18) Sachs, J.P. and J.H. Rushton, Chem. Eng. Progr. 50,597 (1954).
- 19) Van Der Molen, K., Van Maanen, H.R.E., "Laser Doppler Measurements of the Turbulent Flow in Stirred Vessels to Establish Scaling Rules", Chemical Engineering Science, Vol. 33, 1161-1163, 1978.
- 20) Weetman, R.J., Salzman, R.N., "Impact of Side Flow on Mixing Impeller", Chemical Engineering Progress, 70-74, June 1981.
- 21) Weetman, R.J., Oldshue, J.Y., "Power, Flow and Shear Characteristics of Mixing Impellers," 6th European Conference on Mixing, 1,7, May 1988.
- 22) Wolf, D. and Manning, F.S., "Impact Tube Measurement of Flow Patterns, Velocity Profiles and Pumping Capacities in Mixing Vessels," The Canadian Journal of Chemical Engineering, 137, 139, 141, June 1966.
- 23) Zipp, R.P., "Light Scattering Measurements of Turbulence and Concentration in a Stirred Tank Reactor," Thesis, 1981.
- 24) "Proceedings of the 3rd European Conference on Mixing, April 4 - 6, 1979", British Library Cataloging in Publication Data, Volume 1, 37 - 60, 325 - 336, 1979.
- 25) "Proceedings of the 3rd European Conference on Mixing, April 4 - 6, 1979", British Library Cataloging in Publication Data, Volume 1, 37 - 60, 325 - 336, 1979.